An Open Loop Feed-Forward Control Scheme for Bioinspired Artificial Hair Cell Sensors

Kevin M. Crowley

Thesis submitted to the Faculty of the
Virginia Polytechnic Institute and State University
in partial fulfillment of the requirements for the degree of

Master of Science
in
Mechanical Engineering

Donald J. Leo, Chair
Pablo A. Tarazaga
John W. Grant

12th February, 2015
Blacksburg, Virginia

Keywords: Bioinspired, Lipid Bilayer, Cochlear, Sensor, Artificial Hair Cell, Control, *dSpace*®, *Simulink*®
Copyright 2015, Kevin Michael Crowley

An Open Loop Feed-Forward Control Scheme for Bioinspired Artificial Hair Cell Sensors

Kevin Michael Crowley
Virginia Polytechnic Institute and State University

Donald J. Leo, Advisor

ABSTRACT

This research documents the creation and use of an open-loop feed forward control scheme designed to manipulate the DC potential across lipid bilayer membranes in artificial hair cell sensors. Inspired by the human cochlea's non-linear gain phenomenon, whereby the cochlea can increase or decrease the effective gain of the auditory system, this controller is the first step in developing more sophisticated signal processing schemes for use with future bio-inspired artificial hair cell development. This open-loop controller allows for three preset gain mappings to tailor the DC offset in response to an external stimulus. Linear, non-linear, and sigmoidal mappings were created to observe the differences in system response during constant frequency and variable frequency excitation. In constant frequency testing, artificial hair cell sensors were excited at 100 Hz across a range of input intensities to observe current output response during increasing or decreasing excitation levels. Results showed average coherence values above 0.98 for the relationship between current output and fluid velocity, indicating a strong correlation between excitation and measured output. In the bilayer with stereocilia test case, RMS power increased with higher excitation levels but the various control laws did not appear to have any discernible impact on output power. In variable frequency testing, sensors were excited from 0-300 Hz to observe the real time effects of our control law on amplification or attenuation of output current with varying input intensity. Results of the variable frequency excitation could not definitively prove that

the varied DC potential had an effect on current output due to excessive capacitive noise, but the controller did provide some encouraging results from its behavior during testing. We observed three distinct DC potential response curves for each mapping, indicating, that with some refinement, we should be able to manipulate output current with user defined gain tunings.

To Kaitlyn, Mom, Dad, and Big Brother

Acknowledgments

Before I begin my thesis, I would like to thank those who have helped me achieve so much. First and foremost I would like to thank my family for always believing in me. To my wife Kaitlyn, your hard work, love and support could not be overstated. To my parents, your continued confidence in my abilities has meant so much along the way; and to my brother, our many Skype and League sessions were invaluable these past few years. I would also like to thank Dr. Don Leo for providing me with the opportunity to work alongside him and his colleagues, guiding my research, and for his financial support along the way[1]. Without him, this work would not be possible. Additionally I would like to thank the rest of my committee, Dr. Grant and Dr. Tarazaga, for allowing me to work with their students, use their labs, and for being great resources in this endeavor. Finally, I would like to thank my many friends along the way. To the rest of the guys in the lab, best of luck finishing your work and I look forward to reading about your successes soon.

KEVIN CROWLEY

Virginia Polytechnic Institute and State University

19th January, 2015

[1]The author would also like to acknowledge financial support offered through ICTAS (TSTS-11-48).

Table of Contents

Table of Contents **vi**

List of Figures **x**

List of Tables **xvi**

1 Introduction and Background **1**

1.1 Motivation 1

1.2 Cellular Biology and Lipid Bilayers 2

1.2.1 Cell Theory 2

1.2.2 The Cell Membrane and Lipid Bilayers 3

1.2.3 Lipid Bilayers in Engineering 6

1.3 The Auditory System 6

1.3.1 Stages of Signal Processing and Transduction 7

1.4 Cochlear Mechanics 9

1.5 Hair Cell 11

1.6 Research Goals 13

2 Engineering Theory **14**

2.1 Bilayers as a Mechano-Electrical Transducer 14

2.2 Nonlinear Cochlear Amplification 18

2.3 Quantifying Input Excitation 20

2.4 Test Chamber and Hair Cell Physics 21

2.4.1 Test Chamber 21

2.4.2 Stereocilia Mechanics 22

3 Experimental Design **24**

3.1 Component Fabrication 24

3.1.1 Test Chamber 24

3.1.2 Substrate Fabrication 26

3.1.3 Hair Cell Fabrication 29

3.2 Bilayer Formation 31

3.2.1 Bilayer Chemistry 31

3.2.2 Bilayer Assembly 32

3.3 Testing Procedures 35

3.3.1 Testing Equipment 35

3.3.2 Testing Breakdown 35

3.3.3 Testing Commonalities 36

3.3.4 Constant Frequency Testing 38

3.3.5 Variable Frequency Testing 40

3.4 Control Scheme 41
3.4.1 Controller Hierarchy 41
3.4.2 Control Software 43
3.4.3 User Interface 51
3.5 Data Analysis 53
3.5.1 Time Averaging 55
3.5.2 Fast Fourier Transforms 55
3.5.3 Filtering 55
3.5.4 Spectral Analysis 56

4 Results and Discussion **58**

4.1 Constant Frequency Results 58
4.2 Variable Frequency Results 66

5 Summary and Conclusions **72**

5.1 Summary of Work 72
5.1.1 Hair Cell and Testing Environment 72
5.1.2 Controller 73
5.2 Future Work and Improvements 74

A Test Chamber Specifications **76**

B Miniaturization Work **79**

Bibliography **83**

List of Figures

1.1 Two aqueous droplets containing phospholipids are contained in an oil medium. The phospholipids orient themselves in such a way that the hydrophillic polar heads point inwards towards the aqueous solution, leaving the hydrophobic tails pointed outward towards the oil-phase. 5

1.2 Illustration of a lipid bilayer system inside of a living cell. Figure reproduced in accordance with Encyclopaedia Britannica's Acceptable Terms of Use 2015. http://www.britannica.com/EBchecked/media/45550/Intrinsic-proteins-penetrate-and-bind-tightly-to-the-lipid-bilayer [1] 5

1.3 Simplified illustration of the auditory system, broken into three sections. Figure reproduced in accordance with Encyclopaedia Britannica's Acceptable Terms of Use 2015. http://www.britannica.com/EBchecked/media/536/The-mechanism-of-hearing [1] 7

1.4 (a) Simplified drawing of an inner hair cell. (b) Inner hair cell experiencing movement of stereocilia, resulting in polarization and generation of action potential. 12

2.1 Process of forming a DIB or droplet interface bilayer. a) Two aqueous droplets are separated in an oil phase, allowing for lipid monolayers to form at the interface of oil and water. b) Droplets are pushed together, allowing the monolayers to expel the oil between them and "zip" together. 15

2.2 The equivalent electrical circuit for a lipid bilayer membrane. C_B represents the bilayer capacitance, R_B represents the giga-ohm bilayer seal, an R_S represents the resistance of the aqueous solution. 16

3.1 An exploded view of all components required for the construction of the test chamber. 25

3.2 An example three channel substrate. Lipid bilayer formation can occur in each of the three channels using micropipette manipulation. Rubber gaskets are used to prevent accidental leakage of hexadecane oil around the pipette. . 27

3.3 Top: A side profile of the test chamber with oscillating stereocilia inside. Hexadecane fluid is excited by the stinger which is driven by the modal shaker. Bottom Left: Orientation of the bilayer perpendicular to fliud flow. Bottom Right: Orientation of the bilayer parallel to fluid flow. Both: The red line indicates the plane in which the lipid bilayer is formed, orange circles indicate stereocilia, and the gray rectangles are the micropipette electrodes. 28

3.4 Several steps in the hair cell fabrication process. (a) Concave hydrogel shape cured inside one of the glass pipettes. (b) Polyurethane mold used to shape hydrogel into a small cylinder. (c) Placement of the glass stereocilia. (d) Final hair cell structure composed of a stereocilia embedded in a small hydrogel volume, connected to the pipette electrode. 31

3.5 An example of what the chamber looks with a hair cell sensor inside, prior to filling with hexadecane oil. 33

3.6 Two aqueous droplets surrounded in hexadecane oil prepare to be brought together to form a bilayer. Both droplets are supported by PEG-DMA hydrogels. 34

3.7 A visual breakdown of all tests performed on the artificial hair cell sensors. Note that the constant frequency tests are run at 11 discrete voltage levels while the variable frequency tests are run at one single voltage level. 36

3.8 (a) A high level view of the testing set-up. The test chamber is fixed to an acrylic sheet, resting above the microscope objective for bilayer positioning. The modal shaker and load cell are to the right of the chamber. (b) A closer view of the testing stage. Modeling clay was used around the base of the chamber to help dampen unwanted vibrations that may have been accidentally transmitted to the chamber. 37

3.9 (a) A time domain representation of a linear frequency sweep and th recorded shaker velocities at various shaker voltages. (b) A simple linear regression showing the relationship between applied shaker voltage to the peak velocities recorded. 39

3.10 A schematic representation of the entire control system. The flow of information through the system is provided via the colored pathways and matching text. "LV" and "LC" denote the laser vibrometer and load cell sensors respectively. 42

3.11 A full view of the controlling scheme represented as block diagrams within *Simulink*®. A) Section responsible for controlling the modal shaker output, test type, and triggers. B) Section responsible for sampling DC offset from the gain subsystem and passing to bilayer. 1) Portion of the controller responsible for receiving and smoothing LC and LV inputs. 2) Conversion of LC and LV inputs from voltages to pressure and velocity respectively. 3) Subsystem responsible for compensating for drift in the load cell measurements. 4) Subsystem responsible for synchronizing the load cell and laser vibrometer inputs. 5) Portion of the controller responsible for sampling the intensity values once-per-period. 6) Subsystem responsible for gathering calibration values for a given experiment. 7) Portion of the controller responsible for generating a DC offset given the input intensity. 44

3.12 Block diagram of the subsystem responsible for drift compensation prior to further processing. 46

3.13 Block diagram of the subsystem responsible for synchronizing the load cell and laser vibrometer inputs prior to multiplication. 47

3.14 Block diagram of the subsystem responsible for establishing the input ranges into the gain functions. 48

3.15 Block diagram of the subsystem responsible for selecting a gain function and computing a DC offset potential. 49

3.16 Visual representation of DC offset mapping curves used as the basis of the control law. 50

3.17 User interface for the controller built with *ControlDesk*©. 52

4.1 Autocorrelation results between 95 and 105Hz for (a) the two cases where no bilayer is present and (b) the two cases where a bilayer is present. Each set has been scaled such that the y-axis is equivalent for plots of the same row, but changes between rows. 60

4.2 RMS current vs Input Intensity for (a) the two cases where no bilayer is present and (b) the two cases where a bilayer is present. 62

4.3 Plot of RMS power vs shaker voltage levels for only the cases where a stereocilia was present. Linear regressions are included for the bilayer with stereocilia case. 64

4.4 Time domain plots of excitation intensity, and current output with DC potential for: (a) No Bilayer No Stereocilia and (b) No Bilayer with Stereocilia cases. 67

4.5 Time domain plots of excitation intensity, and current output with DC potential for: (a) Bilayer without Stereocilia and (b) Bilayer with Stereocilia cases. 68

4.6 Cross power spectral density plots for each test variation. Scaled equally for easy comparison. 69

4.7 Coherence plots for each test case. Scaled equally for easy comparison. . . . 69

A.1 Detailed drawing of the main body for the test environment. It is comprised of an acrylic tube mated to two enplates where the membrane is held in place by a second set of endplates (not pictured). 77

A.2 The "extended" substrate use to contain the artificial hair cell sensors. Countersunk holes provide areas for rubber gaskets to seal the test environment, preventing leaks. 78

B.1 (a) Example of a prototype artificial hair cell structure under Narshige microforge. A hydrogel droplet is cured along the length to form an anchor for aqueous lipid solution (b) A close up shot of another prototype artificial hair cell structure with hydrogel anchor. 80

B.2 Preliminary test set-up involving micro scaled droplets and hair cell structures. 81

List of Tables

4.1 Average Coherence and Standard Deviations for Constant Frequency Tests . 61

Chapter 1

Introduction and Background

1.1 Motivation

Across much of the world today there are many countries who continue to experience growing populations year after year. Unfortunately, ever increasing populations also mean there are more children born who could be affected by various disabilities, and a greater health care need for those who become disabled over time, whether through adverse conditions or simply old age. Hearing disorders are one such disability. In the United States alone, the National Institutes of Health estimate that 2 to 3 out of every 1,000 children born are either deaf or hard of hearing. Additionally, it is estimated that nearly 17% or 36 million US adults report some degree of hearing loss. Age-related hearing loss is though to affect nearly one-fifth of adults between ages 45 and 64, while almost 50% of adults over the age of 75 are thought to experience the same problem [2]. Hearing loss, unfortunately, is not the only problem associated with a flawed auditory system. *Tinnitus* is one example of a different

type of hearing disorder which still affects millions of US citizens. This complication causes a continuous ringing sensation of varying intensities to be experienced, much like one would experience after attending a loud concert.

In addition to hearing disorders there are also vestibular disorders which, due to the intrinsic nature of the two systems (auditory and vestibular), means that there are several additional complications which exist. *Vertigo* is one such example of a vestibular disorder. Of US adults, more than 35% over the age of 40 experience some type of vestibular disorder. Moreover, 4% of US adults report some type of chronic balance problem lasting at least three months. Studies have shown that vestibular disorders alone are responsible for 347,000 hospital days each year, and of these disorders many have limited medical solutions.

With such an obvious need for assistance, we have turned to bio-inspiration to help solve these issues and improve the quality of life for millions across the country and the world.

1.2 Cellular Biology and Lipid Bilayers

1.2.1 Cell Theory

It has been nearly 350 years since Robert Hooke first "discovered" what are referred to today as the building blocks of life or, simply put, *cells*. Observing thin slices of cork under a simple microscope in 1665, Hooke noticed many pore-like structures which, at the time, he described as looking similar to the walled compartments a monk at a monastery would live in [24]. Unfortunately with the limited technology at the time, Hooke was unaware that these compartments were anything more than mere vacancies in his plant tissue, let

alone complex living bodies in themselves. What Hooke had actually seen were the cell walls surrounding the plant cells from which the cork was composed. Nine years later, a scientist by the name of Anton van Leeuwenhoek became the first person to observe living cells using a more refined compound microscope. While the observations themselves were the first of their kind, it would still many years before the scientific theories were proposed regarding these microscopic entities and how they fit into the grand scheme of life.

Matthias Schleiden and Theodor Schwann are the two scientists commonly credited with the formulation of "Cell Theory"[7]. This theory contains three major tenants which have since laid the foundation for the field of cellular biology ever since. Over time scientists continued to make discoveries, eventually reaching a point where cells were shown to contain smaller bodies still. Today these bodies are known as organelles [7].

Much like a human has organs, cells too have "organs" of sorts. The components of a cell responsible for specific functions are known as *organelles*. While all organelles are vital to the function of the cell, this research focuses specifically on the organelle known as the cell membrane and the lipid bilayer from which it is formed.

1.2.2 The Cell Membrane and Lipid Bilayers

The cell membrane is one of the most vital parts of eukaryotic cells and one of the shared features of eukaryotic and prokaryotic systems. It can be thought of in many ways as the cell's skin. In addition to providing some shape and structure, one of it's primary roles is the regulation of what moves in or out of the cell. This is achieved in a variety of different ways such as: active transport, co-transport, diffusion, or osmosis. Some of these transport methods require the assistance of intra-membranous proteins, while others simply

rely on concentration gradients and the selectively permeable nature of the membrane itself. Regardless of the cell's function or unique membrane composition, the membrane is a vital structure in all eukaryotic cells and has been studied in great detail.

The cell membrane is comprised of several classes of molecules: carbohydrates, proteins, and most notably lipids. Within the lipid subgroup there exist even more classifications: phospholipids, glycolipids, and sterols [7]. For the remainder of this work, the term *lipid(s)* will refer specifically to the phospholipid group as they are generally the most abundant class of lipids within the cell membrane. Phospholipids are relatively simple molecules composed of a phosphorus head and a hydrocarbon tail. Yet this simple structure gives rise to one of the most important behaviors of the molecule, its amphiphilic nature. A molecule which is *amphiphilic* has the unique property of containing a polar, hydrophillic region along with a non-polar, hydrophobic region. In the case of the phospholipids, the phosphorus head is the polar hydrophillic region while the hydrocarbon tails are the non-polar hydrophobic region. Because of this amphiphilic behavior, a lipid molecule has the ability to orient itself in the most thermodynamically stable position for its given environment. If this environment happens to be an aqueous solution, the lipids will orient themselves such that the hydrophillic heads point inwards towards the greatest concentration of water while the hydrophobic tails point away. Given enough time, a continuous layer will form at the interface of the polar and non-polar regions. This layer is called a *monolayer*. An illustration of this concept can be seen in Figure 1.1.

In the case of the cell membrane, a *bilayer* exists as the primary structure and boundary between the inside and outside of a cell. It can be thought of as two lipid monolayers oriented in such a way that the hydrophobic tails of each monolayer align, leaving the phosphorus heads pointed towards the more polar regions of the surrounding environment. In the case

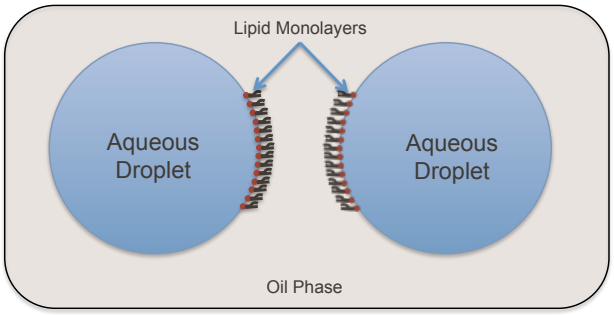


Figure 1.1: Two aqueous droplets containing phospholipids are contained in an oil medium. The phospholipids orient themselves in such a way that the hydrophillic polar heads point inwards towards the aqueous solution, leaving the hydrophobic tails pointed outward towards the oil-phase.

of a cell, the high concentration of water inside and outside of the cell establishes this environment. An illustration of a lipid bilayer as seen in a cell can be seen below in Figure 1.2.

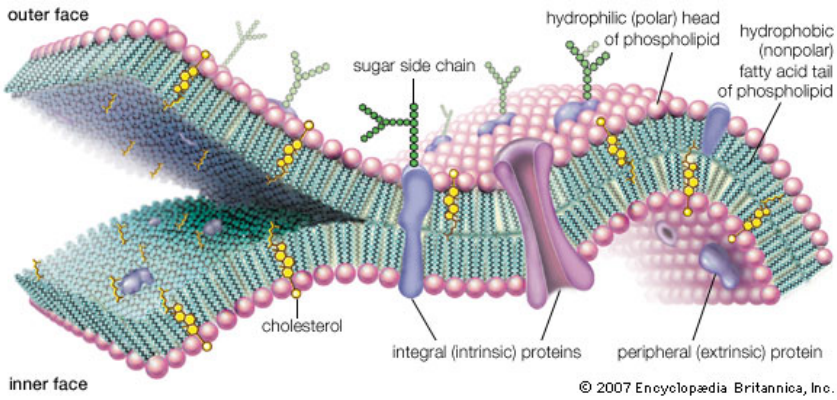


Figure 1.2: Illustration of a lipid bilayer system inside of a living cell. Figure reproduced in accordance with Encyclopaedia Britannica's Acceptable Terms of Use 2015. http://www.britannica.com/EBchecked/media/45550/Intrinsic-proteins-penetrate-and-bind-tightly-to-the-lipid-bilayer [1]

Notice how the bilayer is simply composed of two monolayers joined together to form one structure. This concept forms the basis for how our bilayers are created in the lab.

1.2.3 Lipid Bilayers in Engineering

Lipid bilayers have been a popular subject of study for many scientific disciplines including engineering. Within our group at Virginia Tech Lipid bilayers have been a focus for nearly a decade. With their unique properties, lipid bilayer systems have the ability to act as in a variety of different applications such as artificial hair cell sensors [15, 42, 39, 41, 43, 47, 46], aquatic flow sensors [35], or for use in other smart materials with the incorporation of specific intra-membranous proteins and peptides [33]. In other labs, lipid bilayers have been situated into arrays [4], printed into tissue [49, 52], used to create electrical circuits, bio-networks and beyond [38, 23].

Lipid bilayers have the benefit of being fairly simple and well understood biological structures. They can be drawn upon for bio-inspiration or simply thought of as a dynamic transducer for various smart material applications [40]. Details about the electrical response behavior of lipid bilayer systems will be given later in section 2.1.

1.3 The Auditory System

For the context of this work to be fully understood, it is necessary first to have a brief introduction into the biology of the auditory and vestibular systems. Figure 1.3 gives a high-level overview of the three main sections involved with receiving, transmitting, and processing sound.

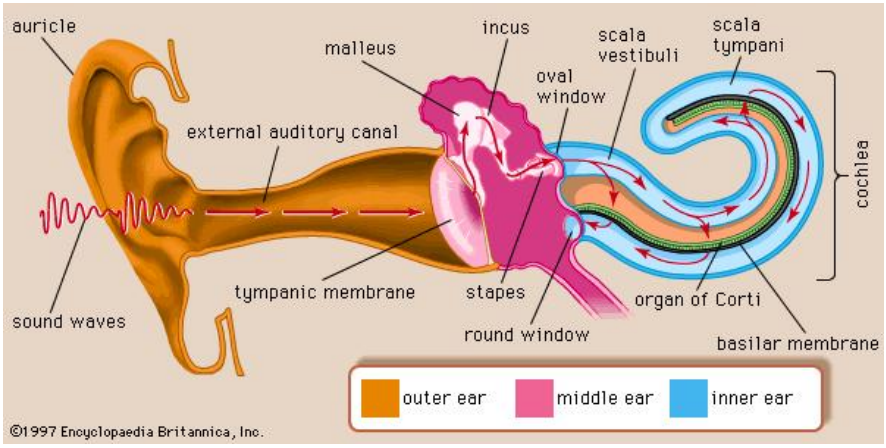


Figure 1.3: Simplified illustration of the auditory system, broken into three sections. Figure reproduced in accordance with Encyclopaedia Britannica's Acceptable Terms of Use 2015. http://www.britannica.com/EBchecked/media/536/The-mechanism-of-hearing [1]

1.3.1 Stages of Signal Processing and Transduction

Outer Ear

The outer ear is the portion of the auditory system up to the *tympanic membrane* or ear drum. It acts primarily as a receiver, whereby sound waves come into contact with the *pinna*, and are then are reflected inward to the *auditory canal*. The physical structure of the outer ear is such that some additional information such as the direction of the sound can also be gathered before moving onward to the middle ear [5]. While the outer ear plays a crucial role in "gathering" sound, it was not the focus of this work. For now, specifics related to its shape and ability to help decipher directional information are withheld. Simply understanding it's role is sufficient for our purposes.

Middle Ear

The middle ear is the portion of the auditory system responsible for transmitting vibration from the *tympanic membrane* to the cochlear fluid via the *oval window*. Composed of three small bones, or ossicles, the middle ear amplifies the incoming sound waves from a relatively low pressure to a much higher pressure. Because the vibration must move from a gaseous medium to a liquid medium in the cochlea, this amplification is required for the next portion of the system to function properly. According to Wever et al., if sound waves were to reach the inner ear directly, bypassing the middle ear, the impedance mismatch would be equivalent to a 30-dB loss of power or energy reflection of 99.9% [5, 50].

Inner Ear

The inner ear is where the incoming sound waves are finally converted from mechanical waves to electrical impulses. It is also the most complex stage of the auditory system. The inner ear is centered around one main structure known as the *cochlea*, which will be described in detail in section 1.4. The cochlea is a snail-like structure responsible for the decomposition of the mechanical stimulus into a frequency map [8, 31, 36]. Further still, within the cochlea are additional structures that assist in processing, and ultimately transducing the incoming mechanical stimulus. One such structure, the *organ of Corti*, is composed of a cellular matrix which runs along the spiraling length of the cochlea [31]. Contained in this "matrix" are two sets of hair cells, outer hair cells (OHCs) and inner hair cells (IHCs). Structurally, the two types of cells are similar; the tasks for these cells though, are very different.

The outer hair cells are primarily involved in amplifying the motion of the basilar membrane in which they are embedded. This motion is a direct result of the incoming mechanical

stimulus associated with sound waves. Each cochlea typically contains three rows of OHCs, yielding approximately 12,000 cells total [5, 8, 31]. These cells respond to changes in their membrane potential by altering their length upwards of 4%, which in turn, amplifies the movement of the basilar membrane. Due to the electrical and mechanical coupling of this system, these cells have the ability to act as a feedback system for the organ of Corti [32, 6, 3].

Eventually the mechanical stimulus, which began as relatively low pressure sound waves in air, is finally interpreted by the inner hair cells. We now elaborate on the specifics of cochlear mechanics, followed by more detail on the inner hair cells.

1.4 Cochlear Mechanics

As we alluded to earlier in the inner ear portion of section 1.3, the cochlea is a complex structure with multiple components that allow it to function as frequency analyzer. The mammalian cochlea is comprised of three main "tubes," known as the: *scala vestibuli*, *scala media*, and *scala tympani*, coiled into a snail like structure [5]. Separating the scala media and scala tympani is a structure known as the *basilar membrane*, and along the length of this membrane is another structure known as the organ of Corti to which we referred to earlier. Contained within the organ of Corti are the inner and outer hair cells from section 1.5.

As the mechanical waves enter the cochlea from the middle ear, a pressure gradient between sections of the cochlea develops along the basilar membrane which begins to vibrate. However, the mechanical properties of the basilar membrane are such that its resonant frequency changes along its length. The stiffer and narrower basal end resonates at higher frequencies, while the less stiff and wider apical end resonates at lower frequencies. Depending on the

excitation received, specific parts of the basilar membrane will vibrate with much higher amplitudes than anywhere else along its length corresponding to the appropriate resonant frequencies.

As the basilar membrane moves, so too does the organ of Corti. While the organ of Corti is a bit more sophisticated, for our purposes we can focus on three main components. Namely, the *tectorial membrane*, *reticular lamina*, and the hair cells themselves. The hair cells are embedded in the reticular lamina which rests above the basilar membrane but below the tectorial membrane. Vibrations in the basilar membrane force the hair cells embedded in the reticular lamina to move accordingly. This is where the difference between outer and inner hair cells comes into play. Stereocilia of the OHCs extend upward from the apical end of the hair cell, coming into contact with the tectorial membrane. Stereocilia from the IHCs merely extend into the fluid filled gap between the reticular lamina and tectorial membrane. Contact made by the stereocilia of the OHCs induces additional mechanical amplification locally, allowing the corresponding inner hair cells to receive additional stimulation. The viscous drag induced by the fluid passing over the stereocilia of the IHCs causes spring-like tip links of the stereocilia to open or close channels of the cell to cations in the surrounding fluid. This induces the hyper- or hypo- polarization of the cell body. In turn, an action potential is generated and passed along to the corresponding neurons which bring the signal to the brain.

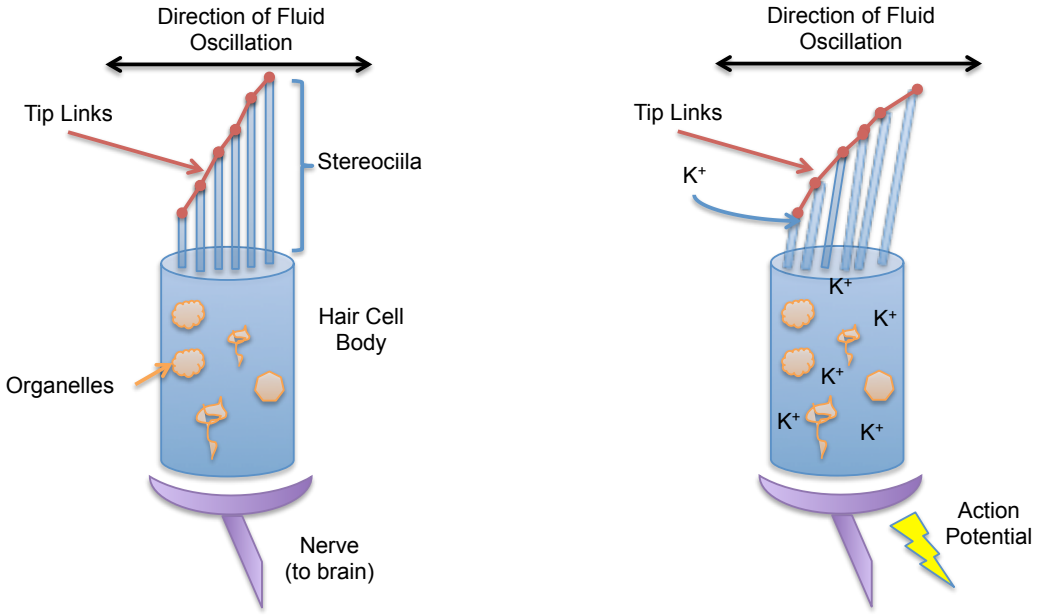
While this process is impressive in its own right, the cochlea has additional capabilities when it comes to signal processing. The one aspect which proved to be the inspiration for this work is the cochlea's capability to actively adjust its response to sound of varying intensities. This will be further detailed in section 2.2.

1.5 Hair Cell

With the general function of the inner ear now explained, we turn to the hair cells of the cochlea. Unlike the hairs on your head, the *hair cells* referred to in this work are actually a very specific type of structure contained within the cochlea responsible for amplifying and detecting the fluid vibrations of the inner ear. While the outer hair cells mentioned earlier have the important function of further amplifying the vibrations within the cochlea, the inner hair cells are the ones responsible for determining the frequency content of the signal. The inner hair cells also function as biological mechano-electrical transducers. They do this by accepting the mechanical vibration which has been processed from both the outer and middle ear, and generating the appropriate action potentials which, in turn, innervate auditory nerves leading to the brain [26, 32, 31, 30, 29, 27, 20, 17, 8, 5, 44].

The structure of the inner hair cell is fairly simple. Like all cells, there is a cell body containing the various organelles required for function. However, unique to these hair cells are structures known as *stereocilia*. These stereocilia are cylindrical protrusions, similar to cantilevered beams, generally grouped into bundles at the apical end the hair cell [26, 11, 32, 14]. Furthermore, the stereocilia are typically different lengths and oriented in such a way that the bundle's profile resembles that of a hypodermic needle, increasing in height from one side to the other. Between tips of these stereocilia there exist structures known as "tip links." These links act as gating springs which can restrict or allow for the flow of cations such as calcium and potassium [8, 26, 32, 14]. Whether or not these "gating springs" activate their respective "gates" is determined by the movement of stereocilia relative to one another within the bundle. The movement of these stereocilia is governed by the relative fluid velocity and displacement of the surrounding fluid within the cochlea. Since the stereocilia and bundle properties vary from cell to cell along the length of the cochlea, the structures

will respond differently depending on the frequency and energy content of the passing fluid. This gives rise to the frequency selectivity of the cochlea. A simplified illustration of an inner hair cell is provided below in Figure 1.4a.



(a) (b)

Figure 1.4: (a) Simplified drawing of an inner hair cell. (b) Inner hair cell experiencing movement of stereocilia, resulting in polarization and generation of action potential.

The influx or restriction of cations into the hair cell allows the cell to hyper- or hypo-polarize. Depending on the direction of polarization, an action potential may be generated by the hair cell which is then transmitted via auditory nerve to the brain. The brain can then resolve the various signals generated by the plethora of hair cells into what we perceive as sound.

1.6 Research Goals

The goal of this work was to expand upon the work of Travis and develop a starting point for tailoring artificial hair cell current output by controlling the DC offset across a lipid bilayer system. Additionally, we aimed to implement this control functionality on an artificial hair cell system contained in a fluid filled environment, to continue working toward the larger goal of developing sensors for use in the mammalian cochlea. To achieve this goal, several challenges needed to be addressed along the way.

First and foremost, a consistent and repeatable method for forming multiple hydrogel supported lipid bilayer membranes was needed. Next, a fluid filled test chamber was required to provide an environment for the sensors more closely resembling that of a mammalian cochlea. Third, a testing method was required to excite the AHC's via external vibration of an elastic membrane attached to the test chamber. Finally, a control scheme needed to be created allowing for the DC potential across the bilayer to adapt, in real time, to the input excitation in accordance with pre-defined mappings. The solutions to each of these challenges will be addressed throughout the remainder of this document.

Several strides were also made in regards to miniaturizing the hair cell structures detailed in this work. While the structures detailed here are still on the order of one millimeter, micropipettes were used to both deposit and interrogate micron-sized aqueous lipid droplets successfully. Additional details of this work can be seen in Appendix B as well as in some of the work by Dunlap.[**?**].

Chapter 2

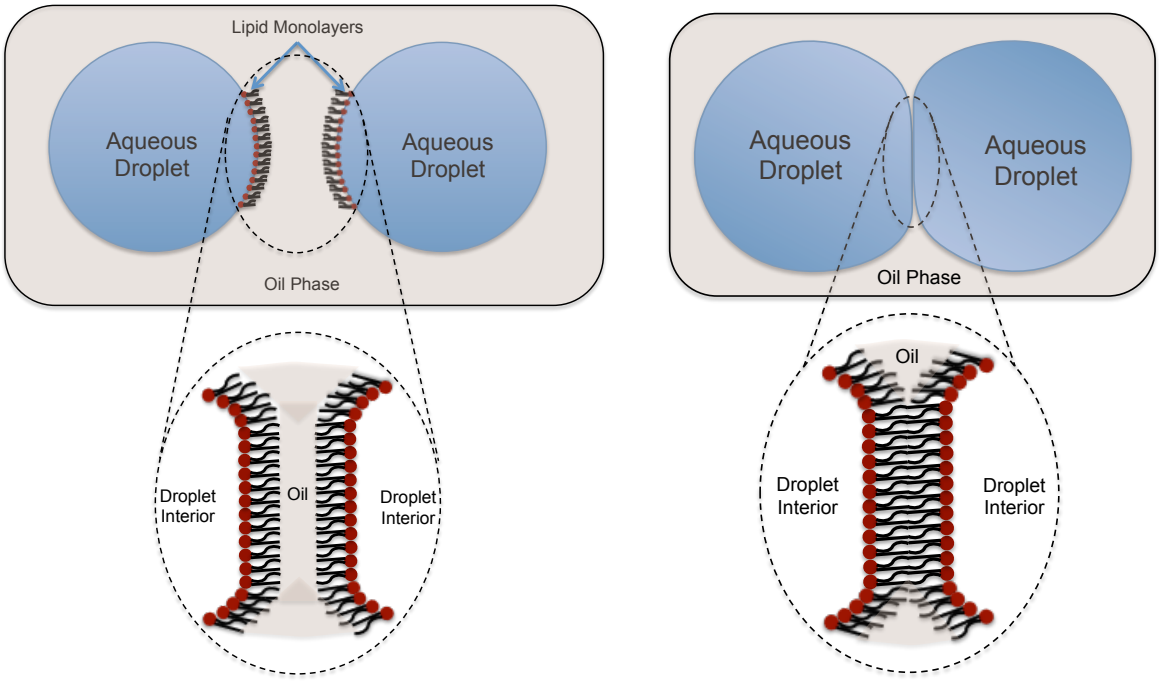
Engineering Theory

2.1 Bilayers as a Mechano-Electrical Transducer

Transducers are devices which simply convert a signal from one form of energy to another, different form of energy. Many different transducers exist for a variety of applications, but for this research we focus specifically on lipid bilayers as mechano-electrical transducers. That is, we input some type of mechanical energy into the system and output a measurable electrical signal. This is possible due to the inherent nature of lipid bilayer systems and their electrical properties.

To form a bilayer for our purposes, two aqueous droplets containing lipids are allowed to idle in an oil medium, facilitating the formation of a single monolayer at the oil/water interface. After monolayer formation, these droplets are brought together, allowing for spontaneous bilayer formation upon expulsion of the imiscible fluid between droplets. An illustration of this process can be seen in Figure 2.1. Specifics of the bilayer chemistry, and manipulation

will be discussed in section 3.2.



(a) (b)

Figure 2.1: Process of forming a DIB or droplet interface bilayer. a) Two aqueous droplets are separated in an oil phase, allowing for lipid monolayers to form at the interface of oil and water. b) Droplets are pushed together, allowing the monolayers to expel the oil between them and "zip" together.

The equivalent electrical circuit for a lipid bilayer system such as the one above, can be represented as a capacitor and resistor in parallel with one another. This illustration can be seen in Figure 2.2.

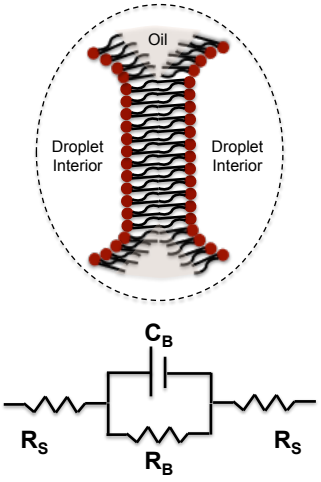


Figure 2.2: The equivalent electrical circuit for a lipid bilayer membrane. C_B represents the bilayer capacitance, R_B represents the giga-ohm bilayer seal, an R_S represents the resistance of the aqueous solution.

As seen above, this circuit is a simple RC circuit with the bilayer's resistance (R_B) and capacitance (C_B) in parallel with resistance from the aqueous solution and electrodes on either side R_S.

As our measurements rely on the current output from this system it is important to know how that current is generated. First we can simplify our equivalent circuit by realizing that R_B is extremely high, on the giga-ohm scale. Thus, we can imagine our system acting as purely capacitive. In a purely capacitive circuit, the charge in the system is governed by the equation:

$$Q = C * V \tag{2.1}$$

where C is the capacitance and V the applied voltage.

Because the definition of current is simply the time rate of change of charge, we can take

the derivative of equation 2.1 to arrive at the following equation:

$$i(t) = \frac{d}{dt}(C * V) \tag{2.2}$$

$$i(t) = V(t)\frac{dC(t)}{dt} + C(t)\frac{dV(t)}{dt} \tag{2.3}$$

We can see then, that the current through our bilayer system is dependent on both the applied voltage and the capacitance of the bilayer. There may also be the presence of an *electrowetting effect*, which can change the bilayer's area depending on the applied potential [51, 22, 34]. This electrowetting effect does not introduce any additional governing terms but instead changes the capacitance, C, from a constant value to one which is dependent on both voltage and time:

$$C(V,t) = C_0(t)(1 + \alpha V^2) \tag{2.4}$$

Substituting 2.4 into equation 2.3 gives us the following equation:

$$i(t) = \Big[C_0(t)(1 + \alpha V(t)^2)\Big]\frac{dV(t)}{dt} + V(t)\Big[\frac{d}{dt}(C_0(t)(1 + \alpha V(t)^2))\Big] \tag{2.5}$$

while computing the derivatives and expanding yields:

$$i(t) = \Big[C_0(t)+\alpha C_0(t)V(t)^2\Big]\frac{dV(t)}{dt}+\Big[\frac{dC_0(t)}{dt}V(t)+2\alpha C_0(t)V(t)^2\frac{dV(t)}{dt}+\alpha V(t)^3\frac{C_0(t)}{dt}\Big] \tag{2.6}$$

Equation 2.6 then is the governing law behind current generation in a lipid bilayer system with a continually varied DC potential. If we assume a constant DC potential as is the case

of our group's previous work, we can simplify equation 2.6 to arrive at equation 2.7.

$$V\frac{dC_0(t)}{dt}(1+\alpha V^2) \tag{2.7}$$

This simplified equation is consistent with the group's previous work and experimental findings, providing a check on the equations above.

2.2 Nonlinear Cochlear Amplification

Of particular interest in this work was the ability of the cochlea to actively amplify low intensity signals, while limiting amplification at higher intensities [3, 8, 18, 31, 30, 19]. This is part of the reason, as humans, we can pick up the slightest whispers while also being able to hear much louder sounds without the degree of amplification remaining constant. Still, there is a limit as to how soft or loud sounds can be before they are outside of our hearing range. For example, we will never be able to discern the sound of atomic collisions. Similarly, we might never be able to stand next to a jet engine comfortably. How the cochlea actively amplifies or attenuates the incoming signals is something both very unique and very useful.

Examples of this cochlear behavior can be seen in the works of Dallos. Using a guinea pig cochlea, Dallos subjected the inner and outer hair cells to a single tone 800 Hz sound of varied sound pressure levels and measured the receptor potentials of said cells. What he observed was an increase in receptor potential from 10 to 60 dB after which the potentials plateaued and began to decrease [9]. In a separate experiment, Dallos measured the amplitude of vibration of another guinea pig cochlea. Dallos tested the response at several frequencies ranging from 3 kHz to 20 kHz, and at sound pressure levels of 20dB, 40dB, 60dB, and 80dB.

As sound pressure levels decreased, he observed a noticeable increase and sharpening of the gain functions for a given excitation frequency. These increases were most pronounced near the corresponding resonant frequency of the basilar membrane and tended to have a much less significant effect when excitations were less than one octave below the characteristic frequency [8].

Dong and Olson have also provided evidence of a sharpened tuning, or gain curves generated by outer hair cell somatic forces which ultimately act as a power amplifier within the cochlea. Stimulating the cochlea of an adult gerbil with pure tones, Dong and Olson measured electrical activity of the outer hair cells as well as pressure and displacement along the basilar membrane. They were able to isolate the driving mechanism behind activation of cochlear amplification, determining that a phase shift in OHC voltage relative to mechanical response would drive the hair cells to begin cochlear amplification. Since this shift occurs very near to the corresponding resonant frequency of the excitation tone, a localized sharpened response was observed [10].

Dr. A.J. Hudspeth is another researcher who has studied active cochlear behavior and the role of hair cells in mammalian hearing. In his review, he simply states that in one experiment, "a threshold stimulus of 0 dB evokes a basilar-membrane oscillation near ± 0.1 nm...the loudest possible sound [like a jet plane or rock concert] measures 120 dB but moves the basilar membrane by only ± 10 nm." For an sound pressure level one-million times greater than threshold, displacement of the basilar membrane increases 100-fold [25, 37]. He too notes the presence of highly-selective frequency tuning characteristics of the cochlea in this work and others.

While many of the details behind the specific mechanisms controlling the cochlea's ability to act as a nonlinear amplifier are still unknown, the behavior has been well documented by a

number of scientists for many years [3, 8, 10, 13, 21, 27, 30, 36, 37]. For our work, we strive to introduce our own method of nonlinear gain to augment the response of our artificial hair cell sensors.

2.3 Quantifying Input Excitation

Before discussing the specifics of experimental design and testing it is important to discuss the underlying variables which drive the controller detailed in section 3.4.

The primary variable with which the controller is governed is called *intensity*. The intensity parameter is a vector quantity which relies on both membrane pressure and membrane velocity and was chosen to be relate-able to the well known quantity of acoustic intensity. Acoustic intensity is simply a measure of the power per unit area of an acoustic signal and is computed by taking the produce of sound pressure and particle velocity $\vec{\mathbf{I}} = p * \vec{\mathbf{V}}$ where $p = p_{total} - p_{ambient}$.

In our case, we use a similar idea but compute intensity by taking the scalar product of membrane pressure and membrane velocity. The difference being that we compute pressure on the membrane by dividing the measured input force of the shaker by physical area of the membrane rather than obtaining a pressure reading of the fluid via hydrophone.

$$\vec{\mathbf{I}} = p * \vec{\mathbf{V}} \quad where \quad p = \frac{F}{A} \tag{2.8}$$

For these tests, the use of a hydrophone was forgone to significantly reduce the complexity

of adding additional instrumentation to the small testing chamber. However, since the system is calibrated prior to testing, the actual parameter used to drive the controller is inconsequential so long as the parameter varies in a known way.

2.4 Test Chamber and Hair Cell Physics

2.4.1 Test Chamber

Prior to this work, the behavior of the hexadecane fluid inside our test chamber was investigated to understand the relationship between input excitation and velocity profile [48]. While the specifics can be found in the referenced material, the resulting analysis showed that given certain assumptions, namely a linear flow field and entrance length less than the distance from our flexible membrane to the stereocilia, the fluid velocity at the stereocilia would be equal at all points along the structure [12, 16, 28]. This velocity is determined by the equation below:

$$V_{stereocilia} = \frac{Q_{in}}{A_{duct}} \tag{2.9}$$

where Q_{in} is the volume velocity at the membrane given by the equation:

$$Q_{in} = V_{stinger} * A_{eff} \tag{2.10}$$

This was worth noting as the effective stinger area, A_{eff}, of previous work, was not quite

the same size or shape of the duct area A_{duct}. This work re-shaped the contacting end of the stinger to make A_{eff} as close to A_{duct} as possible, improving the velocity profile of the fluid flow.

2.4.2 Stereocilia Mechanics

Choosing an excitation frequency for our constant frequency testing, and a frequency range for our variable frequency testing, was an important step taken to try and maximize our sensor response. To achieve the maximum response, we wanted to excite the system at a frequency, or frequencies, close to the resonant frequency of the sensor itself, much like the resonant response of the basilar membrane. To do this, a Rayleigh-Ritz approximation method was used to approximate the first natural frequency of the stereocilia in our artificial hair cell sensor [48]. As we have demonstrated before, this approach provides a reasonable estimate first resonant frequency of the structure. The key assumptions for this approach are as follows:

- The stereocilia structure resembles a tapered beam.
- The hydrogel base of the AHC is not allowed to translate in any direction.
- The hydrogel base of the AHC is allowed to rotate on the axis formed by the micropipette electrode, constrained by a torsional spring.

Since the derivation of admissible functions, system energies, and mass [M] and stiffness [K] matrices are outlined elsewhere, we will forgo the detailed explanation here. After implementing the appropriate assumptions and computing the natural frequencies for our hair

cell geometries we arrive at an estimated first resonant frequency of approximately 100 Hz. Thus, a 100 Hz sine wave was chosen as the excitation signal for our constant frequency testing. For variable frequency testing, we chose a broader frequency range from 0 Hz to 300 Hz. This range encompasses the first resonant frequency while also allowing us to observe the AHC and controller's response at excitation frequencies outside of resonance, also maintaining reasonable excitation intensities from our modal shaker.

In actuality, several of our assumptions could be improved. The tapered beam assumption is close but not identical to the true geometry of the stereocilia being a tapered cylinder. In two-dimensions this is accurate, but an extension to three dimensions could provide additional information. The hydrogel base of the AHC likely also has the potential to translate to some degree. There may also be an additional out-of-plane stiffness term caused by the micropipette electrodes, and mechanical properties of the hydrogel itself could be investigated further. Currently very little literature exists in regards to quantifying these mechanical properties, and even then, small variations from batch to batch may have an effect on the system dynamics as a whole.

Chapter 3

Experimental Design

3.1 Component Fabrication

3.1.1 Test Chamber

Drawing on previous work by Travis, an acrylic chamber was developed to support the testing of several artificial hair cell (AHC) sensors in a fluid filled environment [48]. Acrylic was chosen primarily for its oil resistant and transparent nature, allowing for compatibility with a hexadecane oil phase and the use of optical microscopes. Initial design and assembly work was performed using the Autodesk Inventor 2014 CAD software suite. Upon validation of the design, various sections of the chamber were fabricated from bulk acrylic tubing and sheets through the use of a Universal Laser Systems laser cutter, and Objet rapid prototyping printer. An expanded view of all components can be seen in 3.1[1].

[1]Some details of the aforementioned components may vary from the illustration, such as fastener type.

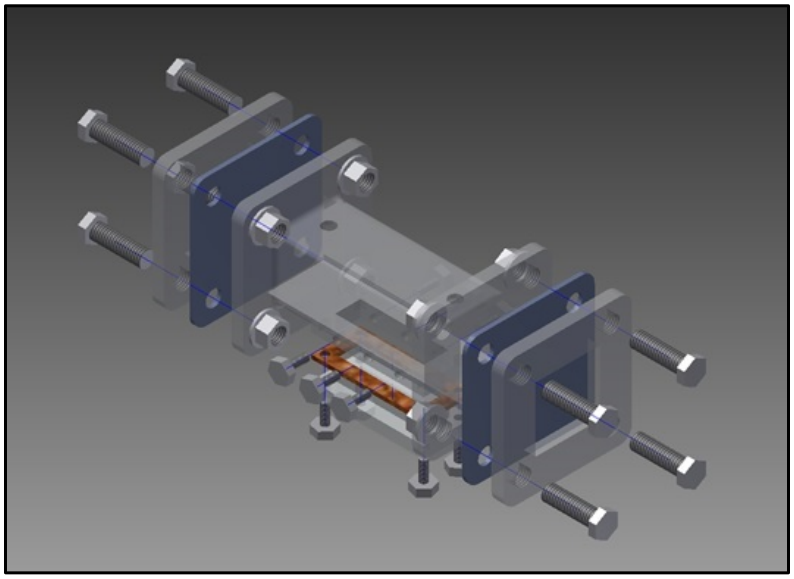


Figure 3.1: An exploded view of all components required for the construction of the test chamber.

Assembly of the chamber was completed using a urethane sealant to bond the tunnel and end plates together, while standard hardware was used to fasten the associated sub-components to the main body. Leak testing of the chamber was performed to ensure air-tight seals throughout, greatly reducing the possibility of air entering the system and compromising the test environment.

While many of the design elements are similar to Travis' chamber, there were two significant changes which merit recognition. The first will be detailed here while the second will follow in section 3.1.2. First, the "flexible membrane," hereby termed *membrane*, used by Travis was composed of a water-clear, flexible polyurethane rubber, ClearFlex 50 (Smooth-On Inc., Easton, PA). In this work, the membrane was substituted with a thin nitrile rubber stretched over the endplates. While the polyurethane material has excellent oil-resistance, the material is both stiffer and less resilient than the nitrile rubber used. When excited by the modal shaker, the polyurethane is more likely to transmit vibration around the testing

chamber as opposed to being directed into the hexadecane medium. This is significant as vibration of the bilayer containing substrate will generate significant current outputs which may be incorrectly attributed to stereocilia oscillation. Additionally, the lower resilience polyurethane does not respond as well to high frequency excitation, reducing the chances that the frequency of the oscillating fluid flow inside the chamber matches that of the input excitation frequency from the shaker. Nitrile rubber also has excellent oil-resistance, but the increased elasticity and higher material resilience improve the chances that the input excitation is more faithfully represented in the hexadecane medium without transmitting unwanted energy around the chamber.

3.1.2 Substrate Fabrication

Crucial to the formation, manipulation, and stability of the bilayer-based hair cell system is the portion of the system hereby referred to as the *substrate*. The substrate provides a physically constrained environment where bilayer formation takes place between the two separate DPhPC volumes. Specifics of the bilayer formation process are given in section 3.2.

As mentioned above in section 3.1.1, there were two key differences from this chamber design and the one used by Travis. The second key difference was the substrate design. The substrate used by Travis was designed to implement the Regulated Attachment Method (RAM) for bilayer formation which has been successfully used by our group for a number of years. This method works well for forming a single bilayer as the compression and relaxation of the polyurethane substrate does not affect neighboring wells. However, if multiple bilayers are desired, the compression or relaxation of the substrate may inadvertently change the size and shape of neighboring bilayers as it expands and contracts. Additionally, this method can be bulky relative to our solution and its implementation is less versatile. As we strive to create

smaller systems the need for more accurate and precise control over bilayer manipulation is also required.

In this work, the substrate is simply a solid ABS plastic piece with three separate channels in which bilayers are formed. Each channel has a small through-material hole with two countersunk holes at each end to facilitate pipette control and prevent leakage with the use of rubber gaskets. By applying a small in-line force, inward or outward, the pipette can be pushed or pulled to a specific location. These pipettes can be manipulated by hand, or attached to several different micro-manipulators for extremely precise control. An example substrate can be seen below in Figure 3.2.

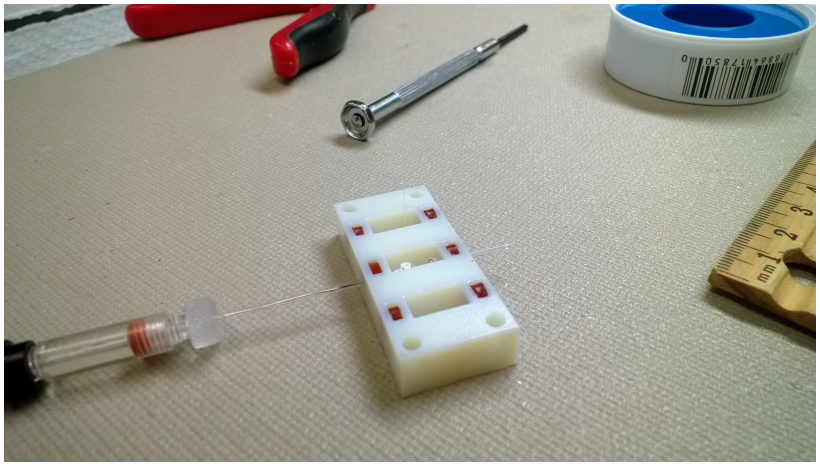


Figure 3.2: An example three channel substrate. Lipid bilayer formation can occur in each of the three channels using micropipette manipulation. Rubber gaskets are used to prevent accidental leakage of hexadecane oil around the pipette.

This piece was fabricated using an Objet Eden 260V rapid prototyping printer, allowing for high precision, accuracy, and quick turnaround. A clear acrylic floor was then attached to the bottom of the substrate with urethane sealant. One potential drawback of using this formation method is the orientation of the bilayer relative to the direction of fluid flow inside the chamber. An illustration is given in Figure 3.3.

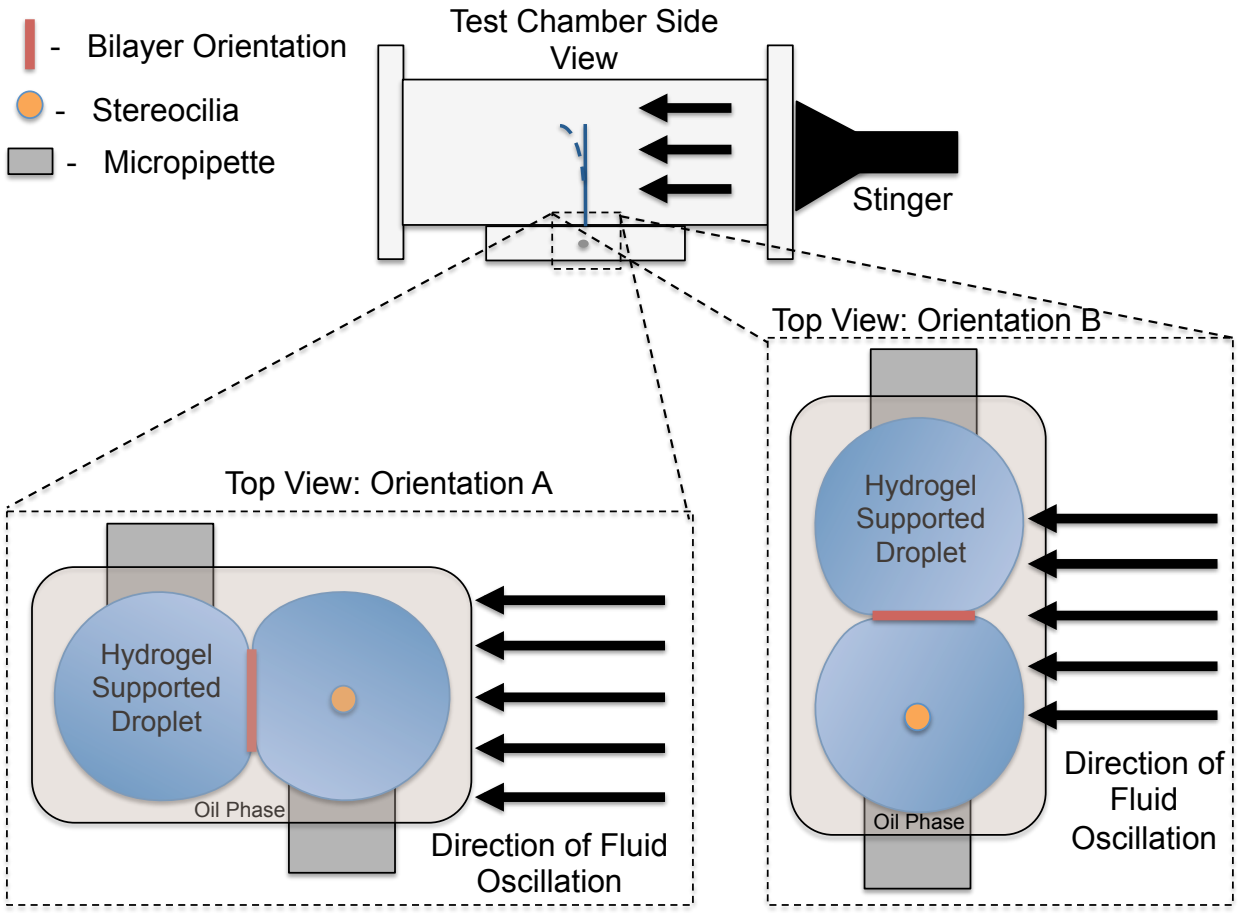


Figure 3.3: Top: A side profile of the test chamber with oscillating stereocilia inside. Hexadecane fluid is excited by the stinger which is driven by the modal shaker. Bottom Left: Orientation of the bilayer perpendicular to fliud flow. Bottom Right: Orientation of the bilayer parallel to fluid flow. Both: The red line indicates the plane in which the lipid bilayer is formed, orange circles indicate stereocilia, and the gray rectangles are the micropipette electrodes.

Unlike many of our previous tests, the bilayer's area lies in a plane parallel to the direction of fluid flow rather than in a perpendicular orientation. This was due primarily to limitations on space and equipment mounting configurations. Sarlo and Tamoddoni have investigated the directionality of bilayer systems in similar orientations and have seen differences in response characteristics. However, both were still able to discern a measurable change in output current during excitation in both orientations [43, 45] As such, we were not overly concerned with this change in orientation.

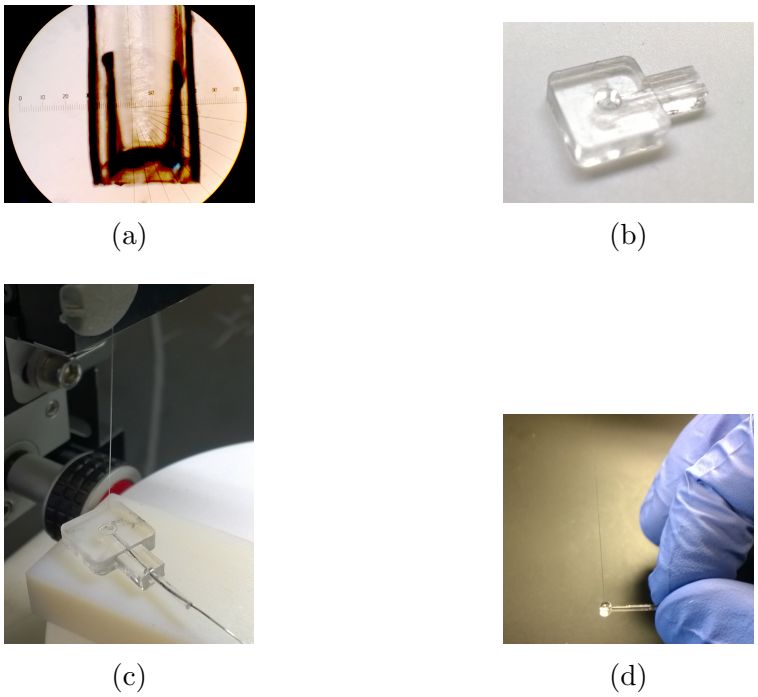
3.1.3 Hair Cell Fabrication

As is the case with much of the previous work in this area, the hair cell used here comprises two separate structures which are then brought into contact with one another, forming a single bio-inspired hair cell unit. This research uses two *hydrogel* supported lipid droplets, with one hydrogel having an embedded glass fiber acting as a stereocilia. Excitation of the fluid surrounding the stereocilia is transmitted down to the hydrogel which then transfers energy to the bilayer, ultimately resulting in measurable changes in electrical current.

The hydrogels described here are a solution of 40% (w/v) polyethylene glycol dimethacrylate (PEG-DMA, MW = 1000g/M, PolySciences, Inc.) with 0.25% (w/v) Irgacure 2959 (Ciba) photoinitiator in 500mM potassium chloride (KCl, Sigma Aldrich), 10mM 4-morpholinepropanesulfonic acid (MOPS, Sigma Aldrich), buffer. While both hydrogel supported droplets are connected to glass micropipette electrodes, the first of the droplets is simply the result of curing a small volume of hydrogel inside the pipette such that it forms a concave lens at one end of the electrode. Once submerged in oil, aqueous lipids are deposited at the same end of the electrode. The combination of hydrogel shape, and surface tension hold the droplet securely on the end of the micropipette electrode in a spherical shape. From here on, this first structure

will be referred to simply as the *supporting pipette*.

The formation of the second structure is more complex. To hold the glass stereocilia, a small cylindrical hydrogel shape was used. First, a water-clear, flexible polyurethane rubber, ClearFlex 50 (Smooth-On Inc., Easton, PA), mold was created to form the hydrogel into the desired geometry. After curing, a glass pipette was inserted while hydrogel was pipetted into the open portion of the mold. Once filled, a small glass stereocilia was held in using a micromanipulator and positioned as close to the center of the mold as possible. Fabrication of the stereocilia was done by heating glass capilaries and allowing gravity to pull them into fiber-like lengths. As such, all stereocilia have a very slight taper along their length. After positioning, the hydrogel is cured. The second structure, from here on referred to as the *follicle*, is then removed. Several steps in this process can be seen in Figure 3.4 on the following page.



(a) (b)

(c) (d)

Figure 3.4: Several steps in the hair cell fabrication process. (a) Concave hydrogel shape cured inside one of the glass pipettes. (b) Polyurethane mold used to shape hydrogel into a small cylinder. (c) Placement of the glass stereocilia. (d) Final hair cell structure composed of a stereocilia embedded in a small hydrogel volume, connected to the pipette electrode.

3.2 Bilayer Formation

The following section will discuss the particulars of bilayer formation in this work. This includes the bilayer chemistry as well as the physical process of forming the bilayers within the test chamber.

3.2.1 Bilayer Chemistry

Forming a lipid bilayer membrane requires two main components: an aqueous solution of lipid molecules and a medium in which they can self assemble. The aqueous solution of lipids

was prepared by combining 2mg/mL 1,2- diphytanoyl-sn-glycero-3-phosphocholine (DPhPC) vesicles (purchased as lyophilized powder, Avanti Polar Lipids, Inc., Alabaster, AL) in a solution of 500mM potassium chloride (KCl, Sigma Aldrich, St. Louis, MO), and 10mM 3-(N-morpholino) propanesulfonic acid (MOPS, Sigma Aldrich, St. Louis, MO), ph 7. This solution was then subjected to five freeze-thaw cycles before being filtered twice through a 0.4 μm Isopore membrane filter (Millipore, Billerica, MA) and two additional times through a 0.1 μm Isopore membrane filter. Filtering was performed using a polypropylene in-line holder (Sterlitch, Kent, WA). This process was completed to increase the homogeneity of the final solution. Bulk solution was stored in a sub-zero freezer at -20°C for up to six months while a small volume of aqueous solution was maintained in a refrigerator for daily use.

The medium for self assembly in this work was hexadecane oil(99%, Sigma Aldrich, St. Lous, MO). Hexadecane oil provides the non-polar environment which is required in conjunction with the polar aqueous solution, facilitating phospholipid orientation for monolayer formation. Additionally, it is a non-conductive medium which ensures current flows only through the aqueous lipid-containing droplets.

3.2.2 Bilayer Assembly

Once the two components used to form the hair cell are completed, they are threaded into one of the available substrate wells. After insertion, the wells are filled with hexadecane oil and a micropipette is used to deposit between 0.5 and 0.65 μL of aqueous lipids onto the end of the supporting pipette. Once deposited,the supporting pipette and follicle are brought into intimate contact to transfer approximately half the aqueous volume from the supporting pipette to the follicle pipette.The result is a single coalesced droplet connecting the supporting pipette to the follicle.

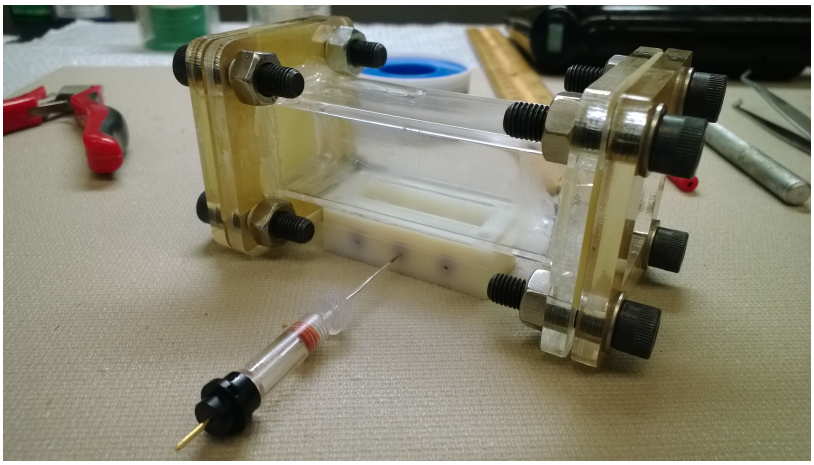


Figure 3.5: An example of what the chamber looks with a hair cell sensor inside, prior to filling with hexadecane oil.

After depositing lipids into each of the substrate wells, the substrate is mated to the bottom section of the test chamber and securely fastened. An example of what the chamber might look like prior to filling it with oil can be seen in Figure 3.5.[2]

Hexadecane oil is then added slowly to the chamber using one of the attached filling tubes until full. The filled chamber is placed on the microscope stage where the supporting pipette is carefully moved away from the follicle, separating the one coalesce droplet into two individual aqueous droplets. Alternatively, the pipettes can be separated prior to filling the chamber which can sometimes reduce the chance of dislodging the aqueous lipid droplet.

These droplets are allowed to sit idle for several minutes to allow for monolayer formation at the oil/water interface. An example of two aqueous droplets preparing to be brought

[2]Since the photo was taken, some improvements were made to various components. As such, this photo provides a good idea of the final product used but is not an exact representation.

together can be seen in Figure 3.6.

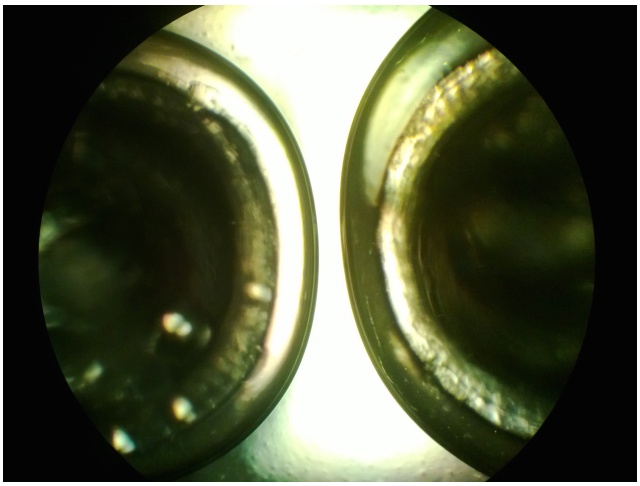


Figure 3.6: Two aqueous droplets surrounded in hexadecane oil prepare to be brought together to form a bilayer. Both droplets are supported by PEG-DMA hydrogels.

After several minutes, the droplets are carefully brought into contact by moving the supporting pipette. Bilayer formation occurs spontaneously once excess oil is pushed out from between the two droplets. This formation is monitored by recording the increase in current generation as a result of passing a 20mV peak-to-peak triangle waveform through the bilayer. As the bilayer grows, the capacitance increases as a function of surface area.

3.3 Testing Procedures

3.3.1 Testing Equipment

The following equipment was used in the experimental set-up:

- Laser Vibrometer - Polytech OFV 303 Sensor Head
- Modal Shaker - Bruel and Kjaer 810 mini-shaker
- Load Cell - Dytran 1051V1
- Signal Conditioner - PCB Electronics
- Anti-Aliasing Filter - ITHACO 4302 Dual 24dB/Octave Filter
- Agilent 33220A 20MHz Function / Arbitrary Waveform Generator
- Microelectrode Amplifier - Axopatch 200B
- Data Acquisition - Axon CNS Digidata 1440 Low-Noise Data Acquisition System
- Data Acquisition - *dSpace*®

3.3.2 Testing Breakdown

Testing of the artificial hair cell system was performed in two separate phases. One set of tests was focused specifically on constant frequency (CF) excitation of the test chamber while a second set of tests was designed for variable frequency (VF) excitation. During the constant frequency testing, the voltage supplied to the modal shaker could be varied to

generate steady-state input excitations of varied intensities; while the modal shaker during variable frequency testing was supplied a single voltage for all tests.

Both the constant and variable frequency tests contained four subsets of test types with each subset containing yet another five subsets of data. To help illustrate the breakdown of tests, Figure 3.7 outlines the testing approach.

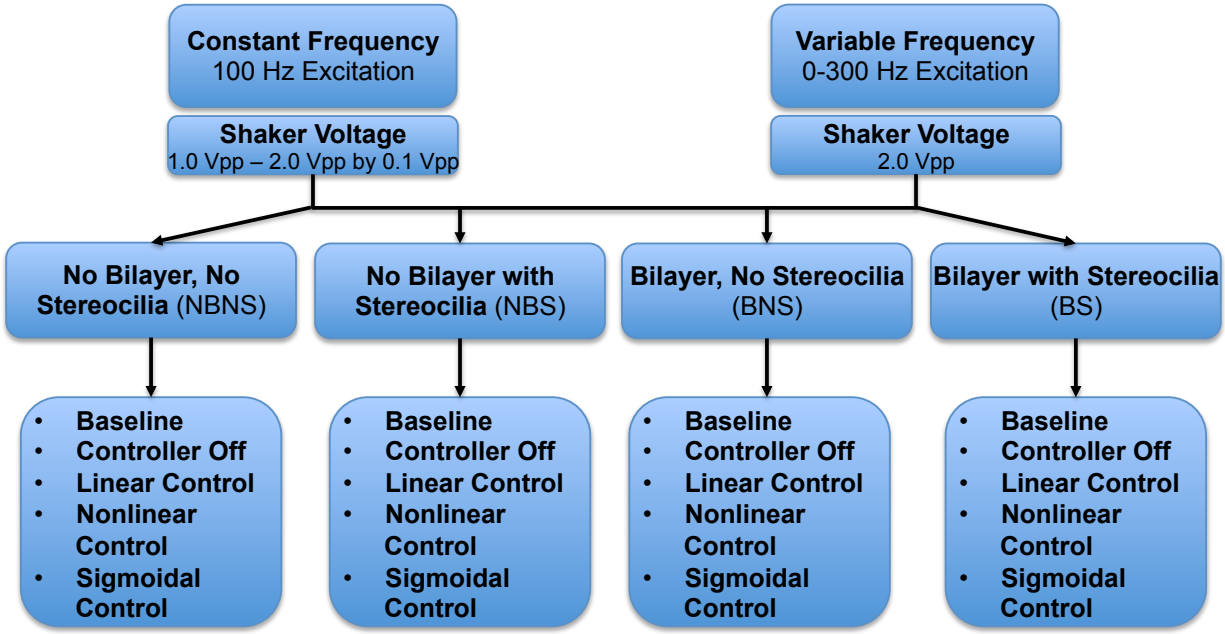


Figure 3.7: A visual breakdown of all tests performed on the artificial hair cell sensors. Note that the constant frequency tests are run at 11 discrete voltage levels while the variable frequency tests are run at one single voltage level.

3.3.3 Testing Commonalities

Aside from the equipment used, there were a few testing similarities between both constant and variable frequency tests. The physical layout of equipment and geometry of the laser vibrometer are two of the most significant commonalities that must be noted. Due to physical constraints, including the use of a Faraday cage, the laser vibrometer was positioned at a

30-degree angle off-center from the modal shaker's line of action. To compensate for this angle, simple geometric calculations were used to ensure that the measured stinger velocity was adjusted to output the horizontal component of velocity only. This is the same set-up first used by Travis [48]. We can then compute the horizontal component of displacement and velocity simply by multiplying the resultant velocity by the cosine of the angle between chamber and vibrometer: $V_R * cos(\theta)$ where V_R is the resultant velocity measured by the laser vibrometer, including both x and y components.

Shown below in Figures 3.8a and 3.8b are actual view of the physical test setup. The laser vibrometer is not pictured.



(a) (b)

Figure 3.8: (a) A high level view of the testing set-up. The test chamber is fixed to an acrylic sheet, resting above the microscope objective for bilayer positioning. The modal shaker and load cell are to the right of the chamber. (b) A closer view of the testing stage. Modeling clay was used around the base of the chamber to help dampen unwanted vibrations that may have been accidentally transmitted to the chamber.

Additionally, for tests involving lipid bilayers, the size of the bilayer was adjusted prior to experimentation, minimizing differences in output due to variations in surface area prior to DC offset changes. Bilayers were adjusted such that a peak-to-peak current measurement

of approximately 400 pA was attained when a 20mV peak-to-peak triangular voltage signal was supplied across the bilayer.

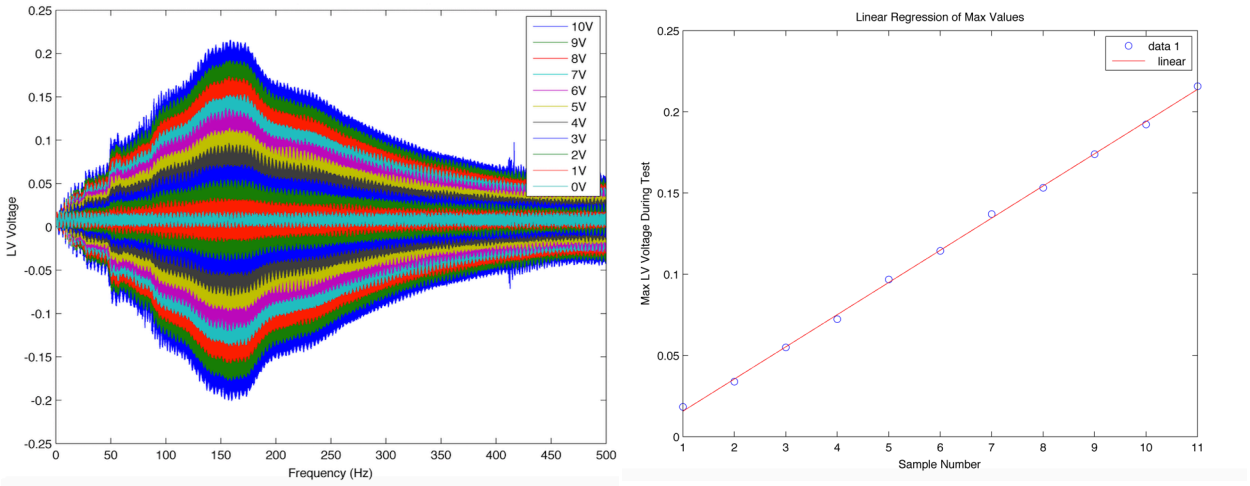
3.3.4 Constant Frequency Testing

Constant frequency testing of the AHC's was performed to investigate the response of the system to various steady state input intensities. These intensities are varied by supplying the modal shaker with several different voltage levels to increase the force and velocity of the stinger on the chamber membrane. Using the Agilent function generator, a 100 Hz sine wave voltage was supplied to the shaker with amplitudes ranging from 1.0 Vpp (peak to peak) to 2.0 Vpp by 0.1 Vpp for a total of 11 discrete voltage levels.

From prior testing, we know that the shaker output velocity has a linear correlation with supplied voltage. Twice the voltage yields twice the output velocity. This is evidenced in Figure 3.9.With this observation, we assumed our intensity calculation would increase linearly with supplied voltage as well.

During the "controller off" portions of testing stepping the shaker voltage to higher amplitudes should then yield overall increases in current output as well. With the control schemes turned on in the cases with a bilayer present, we expect to see some amplification of the signal at low shaker voltages (low intensity) and some attenuation at high shaker voltages (high intensity). This is due to the increased or decreased DC offset potential supplied across the bilayer.

Once the test is prepared there are several steps that need to be taken to correctly execute the test and data collection. These steps are given below:



(a) (b)

Figure 3.9: (a) A time domain representation of a linear frequency sweep and th recorded shaker velocities at various shaker voltages. (b) A simple linear regression showing the relationship between applied shaker voltage to the peak velocities recorded.

1. Choose the correct cut-off frequency on the ITHACO anti-aliasing filter.

2. Set the initial shaker voltage on the Agilent function generator.

3. Set the *Control Desk* software

   (a) Set the control scheme to "Off".

   (b) Clear the previous calibration information in *Control Desk*.

   (c) Verify the sampling rate, test duration, and other experiment parameters.

4. Trigger the shaker to allow automated collection of calibration information.

5. Adjust the desired shaker voltage, and control scheme for the current test.

Each test is carried out three separate times so that any test showing anomalies can be discarded prior to time averaging if necessary.

3.3.5 Variable Frequency Testing

Variable frequency testing of the AHC's is performed to investigate the response of the system to a time-varying intensity. Due to the inherent nature of the modal shaker, output velocity and force vary across a wide frequency ban. For that reason, these tests are performed at a single excitation voltage as varying the supplied voltage would only shift the intensity curve. Since the system is calibrated prior to testing, these shifts become irrelevant during this portion of testing.

The modal shaker is supplied a 2.0 Vpp sine wave ranging in frequency from 0 to 300 Hz over a time span of 30 seconds with a linear rate increase. During the frequency sweep, the input intensity changes over time and the controller modifies it's output accordingly. Thus, when the sampled intensity increases, the DC offset supplied by the controller decreases. Conversely, the DC offset will increase as the sampled intensity decreases. The goal of these tests is to try and maintain an average current level output during the bilayer tests for the duration of the test.

Similar to the constant frequency testing, there are several steps that need to be completed prior to collecting data for the variable frequency tests. They are listed below:

1. Choose the correct cut-off frequency on the ITHACO anti-aliasing filter.
2. Set the shaker voltage on the Agilent function generator.
3. Set the *Control Desk* software
   (a) Set the control scheme to "Off".
   (b) Clear the previous calibration information in *Control Desk*.

(c) Verify the sampling rate, test duration, and other experiment parameters.

4. Trigger the shaker to allow automated collection of calibration information.

5. Adjust the desired control scheme for the current test.

Like the constant frequency portion of testing, each test is carried out three times so outliers can be discarded prior to time averaging if necessary.

The various inputs, switches, and other controls in *Control Desk* are detailed more thoroughly and can be seen in section 3.4.3

3.4 Control Scheme

Critical to this work was the ability to control the gain in the system at low input intensities. Like the cochlea, the goal was to significantly amplify the response of the system at low intensities while simultaneously minimizing amplification at high input intensities. To do this, a feed-forward control scheme was built to continually adjust the gain in real-time as a function of input amplitude.

The control scheme was built using *Simulink*® and implemented with the use of the *ControlDesk*© software provided by *dSpace*®.

3.4.1 Controller Hierarchy

Fundamentally, the control system used is fairly straightforward in regards to the inputs and outputs being received and sent respectively. Figure 3.10 below provides a schematic

overview of the entire system as a whole.

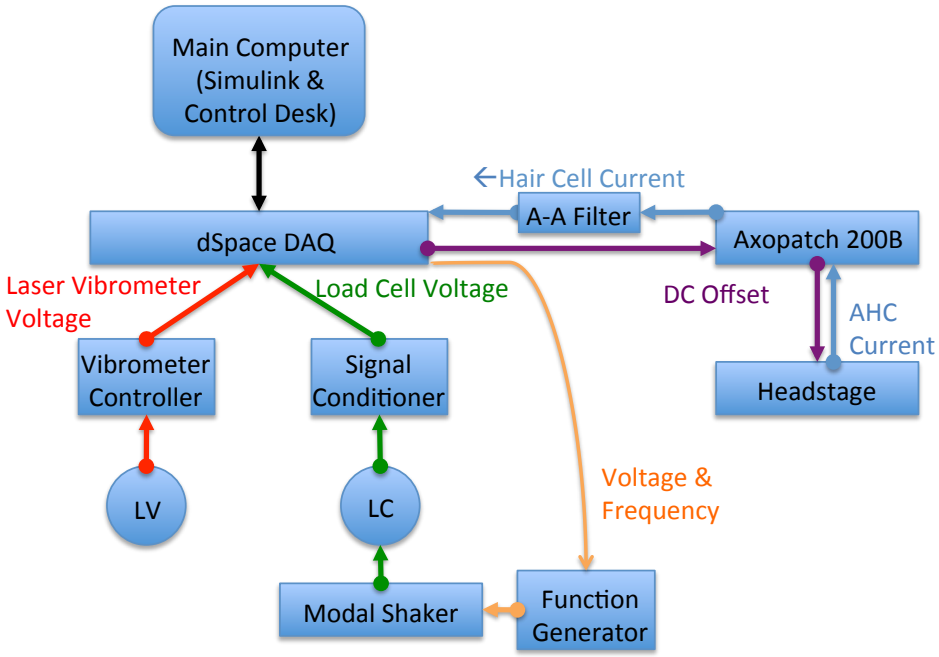


Figure 3.10: A schematic representation of the entire control system. The flow of information through the system is provided via the colored pathways and matching text. "LV" and "LC" denote the laser vibrometer and load cell sensors respectively.

As it can be seen from the figure, there are only three wired inputs to the *dSpace*® controller and two wired outputs. However, there are many additional parameters which can be manipulated within the controller's software. These include the following boolean parameters: triangular wave signal on/off, and control scheme on/off. Additionally there are switches to control: which gain function is used, how the input is normalized, and a reset switch for calibration purposes. These will be further detailed in section 3.4.3.

3.4.2 Control Software

Now that a high-level overview has been given, we look specifically at the various aspects of the software which are processing the inputs and controlling the outputs. It is important to note that the *dSpace*® CP1104 data acquisition system is operating at a sampling frequency greater than twice that of the Axopatch 200B and Digidata 1440 amplifiers, safely above the Nyquist frequency to prevent aliasing by those systems. All signal processing is performed on the "Main Computer" illustrated in Figure 3.10, but some signals are still read by the Digidata system for troubleshooting and verification purposes.

There are three pieces of information received by the computer via the *dSpace*® CP1104 DAQ. The first channel (ADCH5) is reserved for the hair cell current being output from the Axopatch 200B microelectrode amplifier. This input is sent to the main computer simply for recording purposes and has no effect on the DC offset or signals being sent to the bilayer. The second channel (ADCH7) receives input from the Dytran 1051V1 load cell after being passed through the PCB® Piezotronics Model 480E09 ICP® Sensor Power Unit. The third channel (ADCH8) receives input from the Polytech OFV 303 Sensor Head laser vibrometer via the Polytech OFV3001 vibrometer controller. The controller software processes the load cell (LC) and laser vibrometer (LV) inputs and uses them to specify a DC offset which is then sent back to the bilayer. The entire process can be seen in Figure 3.11 with details following.

Upon receiving the load cell and laser vibrometer inputs, the CP1104 DAQ unit divides the signal by '10' and converts the voltages from an analog signal to a digital signal. The signals are then multiplied by '10' in software for computation purposes. Both the LC and LV signals are filtered using an 8th-order low-pass Butterworth filter. These filters were used to

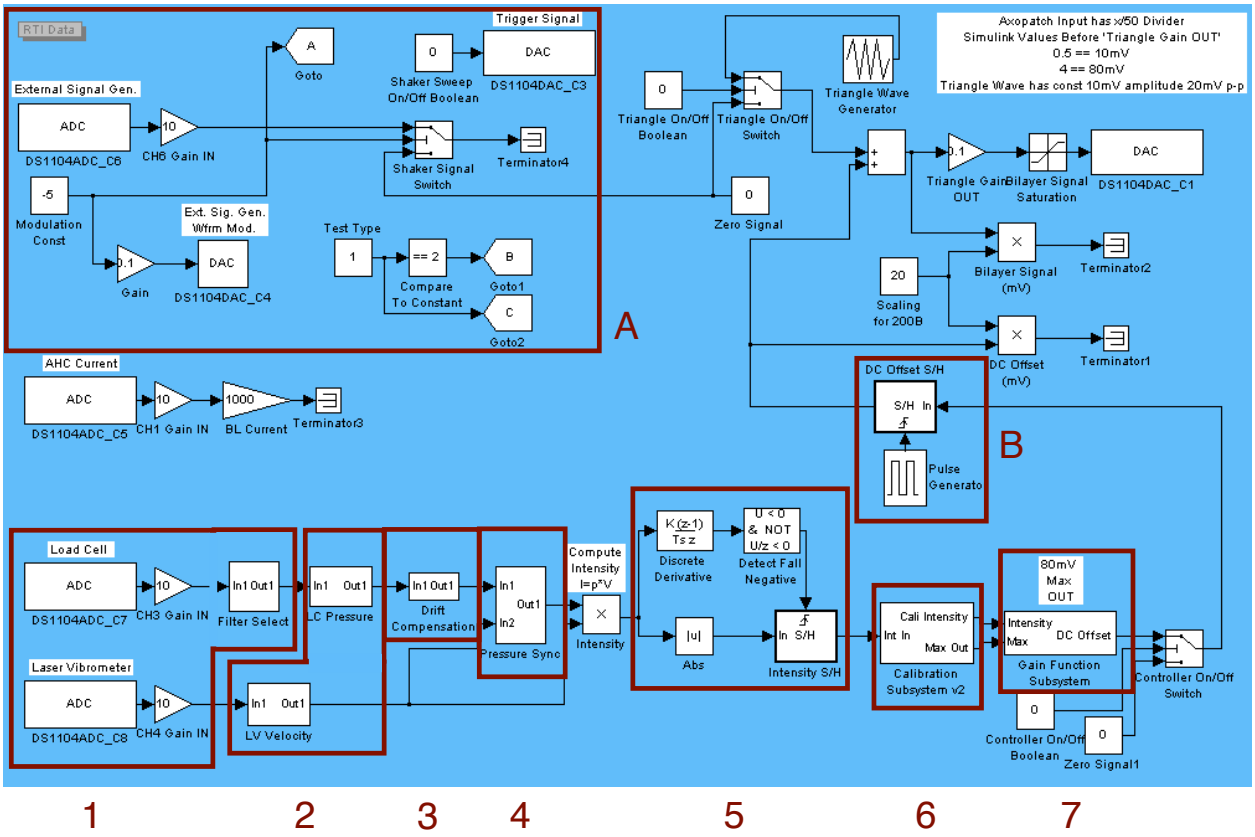


Figure 3.11: A full view of the controlling scheme represented as block diagrams within *Simulink*®.
A) Section responsible for controlling the modal shaker output, test type, and triggers.
B) Section responsible for sampling DC offset from the gain subsystem and passing to bilayer.
1) Portion of the controller responsible for receiving and smoothing LC and LV inputs.
2) Conversion of LC and LV inputs from voltages to pressure and velocity respectively.
3) Subsystem responsible for compensating for drift in the load cell measurements.
4) Subsystem responsible for synchronizing the load cell and laser vibrometer inputs.
5) Portion of the controller responsible for sampling the intensity values once-per-period.
6) Subsystem responsible for gathering calibration values for a given experiment.
7) Portion of the controller responsible for generating a DC offset given the input intensity.

help smooth the input signals, ensuring that the synchronization subsystem would be able to identify the true peaks. These steps correlate to Figure 3.11 step (1). The LC voltage is then converted into units of force (N) via appropriate scaling factors while the LV voltage is converted into units of velocity (m/s). As stated previously, the *intensity* of the excitation is computed by multiplying pressure on the membrane with the velocity of the fluid inside the test chamber. As a result, an additional calculation is performed with the load cell force to determine the approximate pressure exerted on the test chamber membrane. These steps correlate to Figure 3.11 step (2).

During the course of testing, it was observed that there was some degree of drift coming from the load cell which negatively impacted the calibration routines of step 6. To account for this drift, a simple subsystem was built which computed the average of the input each period, compared it with the previous period and added or subtracted the difference. Because the signal is symmetric, the amplitude of the input is preserved while any variations from the zero point are eliminated. This allows for the intensity to continue changing appropriately with increased or decreased loading and stay within the calibration bounds set by the user. This comprises step (3) of Figure 3.11 and is detailed in Figure 3.12.

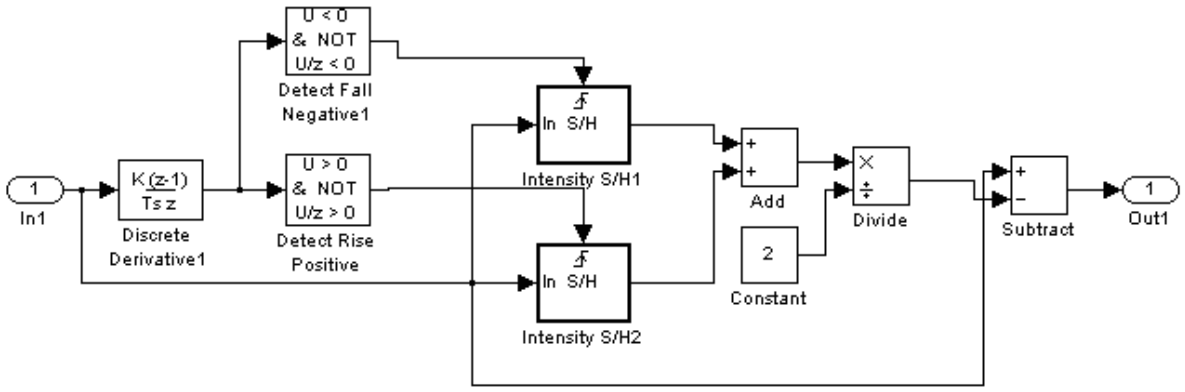


Figure 3.12: Block diagram of the subsystem responsible for drift compensation prior to further processing.

Before multiplying the newly established pressure and velocity, a synchronization process, Figure 3.11 step (4), was required due to a frequency dependent phase shifting between the two signals. To do this, a relatively simple process, shown in Figure 3.13 was used. First, the discrete derivatives of both the LC and LV signals was computed. Given the available toolboxes in *Simulink*® derivative calculations were used to ensure zero-crossings occurred in the signal. There was no guarantee that either sinusoidal signal would oscillate about zero consistently, taking the derivatives of each ensures this crossing. At each negative-to-positive zero crossing of the derivatives (once per period), the simulation time is noted and the difference is computed. This time-delay is then applied to the leading signal to ensure that the peaks and valleys of both the LC and LV signals are consistently in-phase. Other methods to synchronize the signals such as computing the cross-correlation of the waveforms was considered, but ultimately this solution was more computationally expensive and unnecessary.

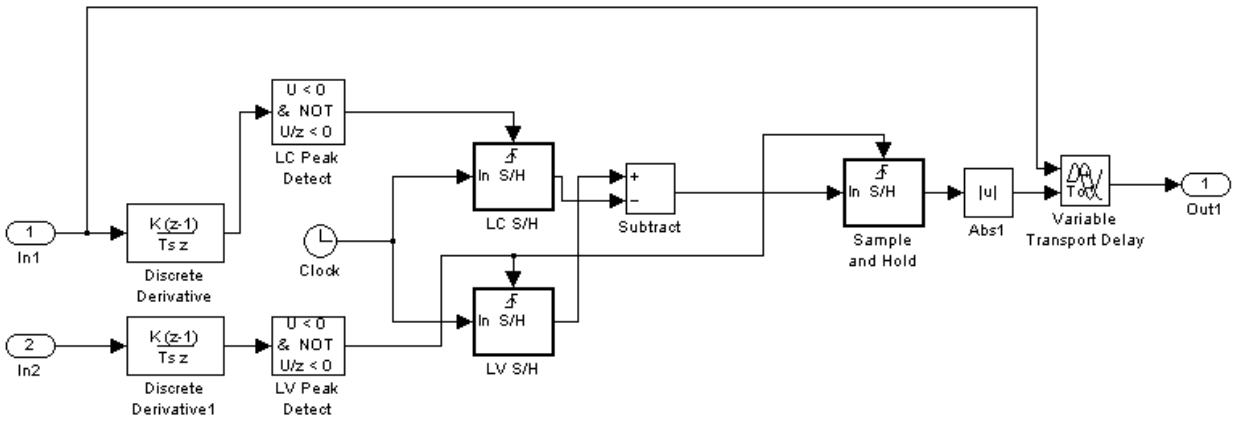


Figure 3.13: Block diagram of the subsystem responsible for synchronizing the load cell and laser vibrometer inputs prior to multiplication.

Once synchronized, the two signals are multiplied together to arrive at an intensity value for use in determining a DC offset. Using a process similar to the one involved in the synchronization of both the LC and LV signals, the intensity value is sampled once-per-period at the peak value. This provides a fairly constant value for use with our gain or offset functions; otherwise, the DC offset of the bilayer would rise and fall as a sinusoid rather than capturing the overall effect of the input excitation. The sampled intensity value is then passed to two separate subsystems. This sampling portion of the controller is highlighted as step (5) of Figure 3.11.

The first subsystem, Figure 3.14, is used for calibration purposes while the second system, Figure 3.15, actually contains the various gain functions. The calibration subsystem functions in a slightly different fashion depending on the type of test being performed. Prior to data collection of the constant frequency tests, the shaker is set to the minimum and maximum voltage states of 1.0Vpp and 2.0Vpp for several seconds. During this time, a running average of input intensity values is computed and set as the upper or lower calibration boundary, providing an expected intensity range that is consistent from test to test and at

each shaker voltage. The ranges are then shifted for computation purposes such that the lower calibration value is set to zero, with the upper bound shifting accordingly.

The variable frequency test captures the upper and lower calibration bounds automatically by running the desired frequency sweep prior to testing. Like the constant frequency calibration, the lower bound is set to zero with a corresponding shift in the upper bound as well. Following calibration of the system the inputs are processed by the gain functions.

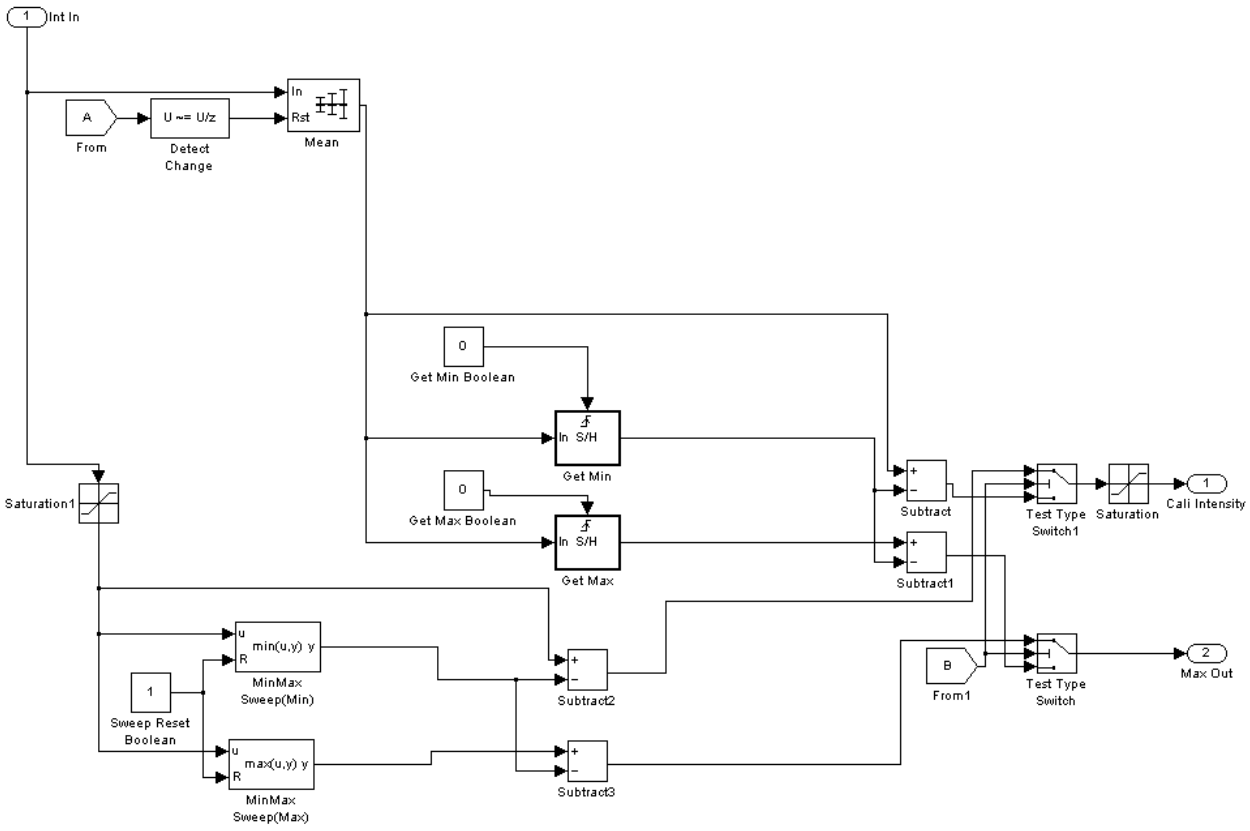


Figure 3.14: Block diagram of the subsystem responsible for establishing the input ranges into the gain functions.

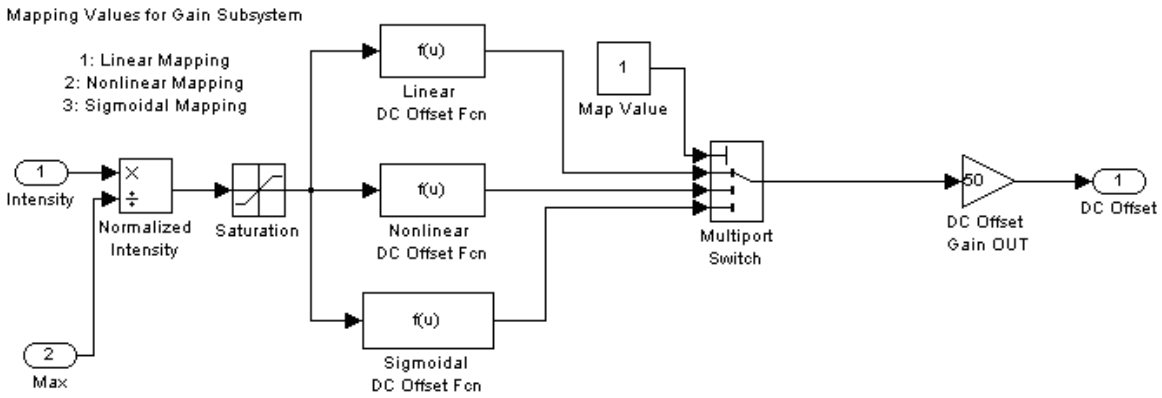


Figure 3.15: Block diagram of the subsystem responsible for selecting a gain function and computing a DC offset potential.

The first step within the gain subsystem is to normalize the inputs.The gain functions were designed in such a way that an input of '1' correlated to the smallest DC offset output or lowest gain. Values less than one lead to subsequently greater amplification via larger DC offsets. After normalization, the intensity signal is passed to one of the desired functions: linear, nonlinear, or sigmoidal. The equations for these functions are given below with a visual representation presented in Figure **??**.

$$Linear : -60x + 60 \tag{3.1}$$

$$Nonlinear : \frac{-120}{1 + e^{-5*x}} + 120 \tag{3.2}$$

$$Sigmoidal : \frac{60}{1 + e^{10}(e^{-20x})} + 60 \tag{3.3}$$

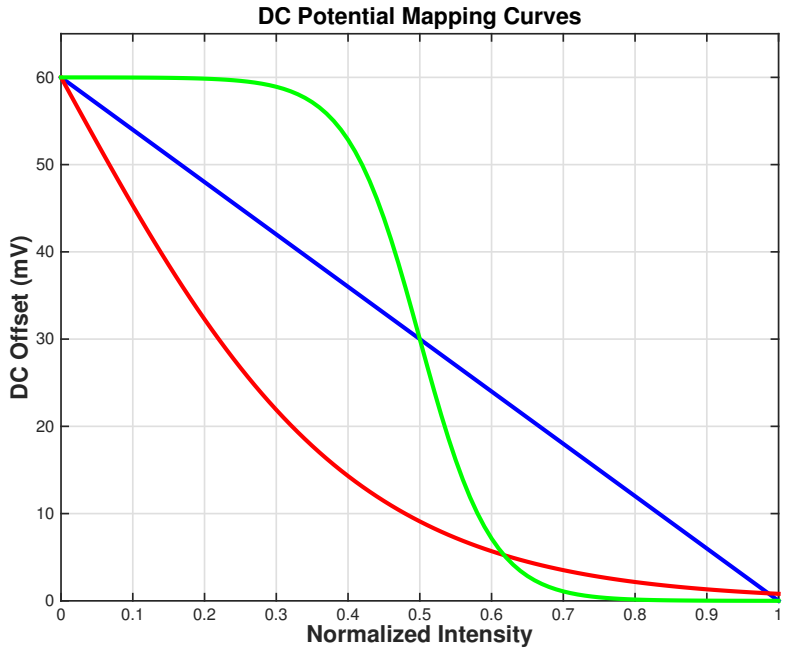


Figure 3.16: Visual representation of DC offset mapping curves used as the basis of the control law.

Each equation is designed to output a DC offset between 60mV and 0mV depending on the magnitude of the intensity. 60mV was selected as a ceiling as DC offsets higher than 60mV can cause the bilayer to rupture prematurely. A DC offset of 0mV leads to zero additional amplification of the hair cell current as desired.

After a DC offset has been computed by one of these functions, it is sampled at a frequency of 4Hz in an attempt to minimize the introduction of jump discontinuities in the signal while maintaining sufficient tracking of the intensity variation. With the governing equation for bilayer current a function of $\frac{dV}{d(t)}$, jump discontinuities in the signal lead to large instantaneous current spikes which create noisy data and threaten to rupture the bilayer. The DC offset is finally output back from the *dSpace*® unit to the Axopatch 200B whereby it is sent to the bilayer via the connected headstage. For the purpose of verifying bilayer formation, a triangular waveform with a 10mV amplitude can also be sent through the same channel with

or without a DC offset. This allows for the observation of bilayer growth and quality via square-wave current measurements.

3.4.3 User Interface

With the controller fully detailed, we now look at the user interface for the system which is built with the *ControlDesk*© software. Within the controller GUI there are multiple plots, displays, switches, and status lights. These objects allow for complete control, observation and measurement of the artificial hair cell system. This user interface can be seen below in Figure 3.17.

If we organize the GUI into six sections, we can detail the various items in each section more easily. Starting in the upper left, we have a plot for the DC offset signal being applied to the bilayer as well as four numeric displays which provide various information. These boxes display the instantaneous intensity measurement and applied DC offset, as well as the running mean intensity for the test and what percentage of the calibrated maximum value the mean value corresponds to. In the upper-middle we have a single plot to display the AHC current measurement.

The upper-right contains several switches and controls. First we see two on/off switches for "Tri. Wave" and "Controller." The "Tri. Wave" switch turns the 20mV peak-to-peak triangular waveform on or off during the bilayer formation and verification phase of testing. It has a visual indicator below. The "Controller" switch dictates whether the control scheme is being used to apply a DC offset to the system. In the "off" state, no DC potential is applied at any point. In the "on" state, the DC potential is governed by the subsequent mapping function. The next set of switches and indicators allows the user to change the controller

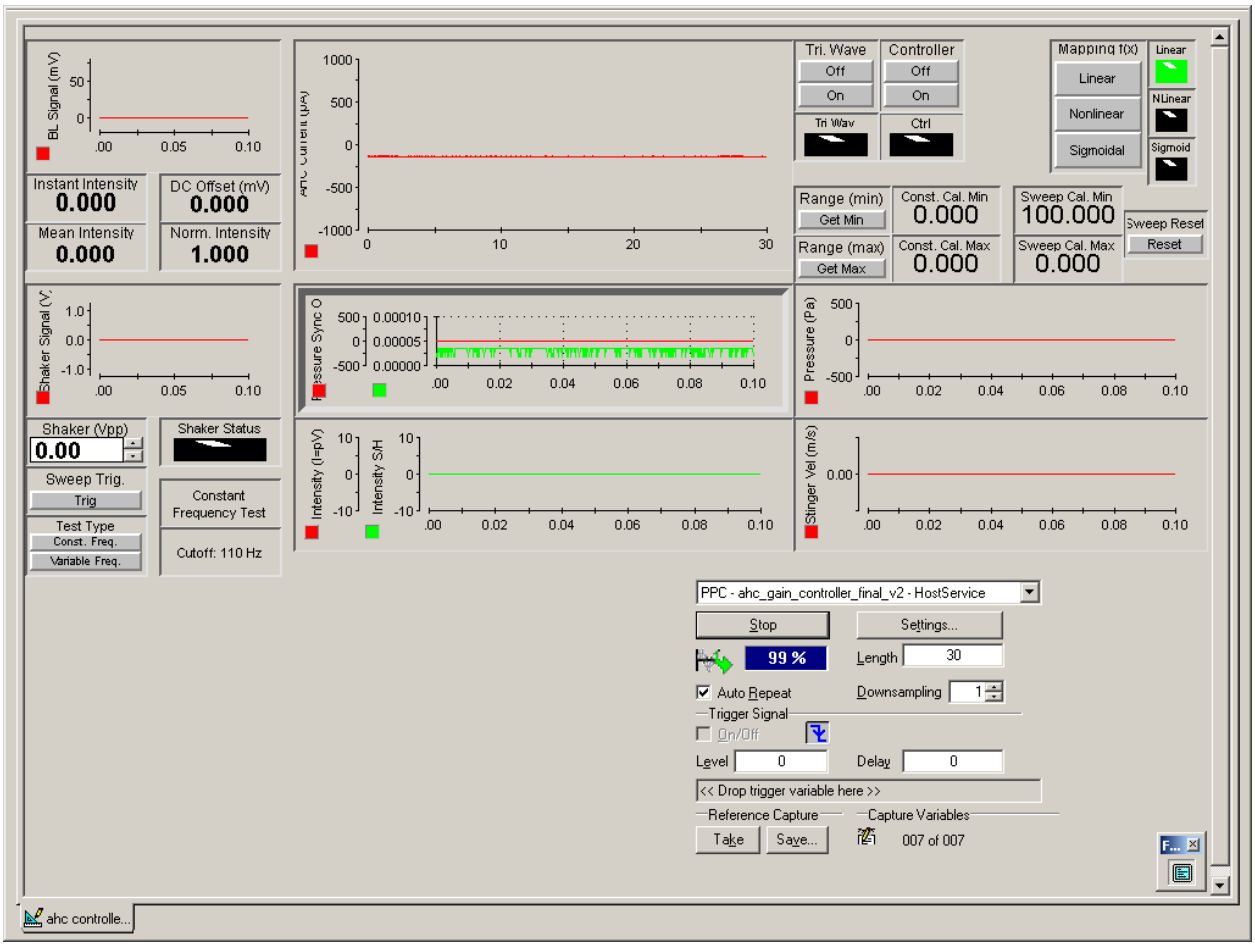


Figure 3.17: User interface for the controller built with *ControlDesk*©.

mapping function from "Linear," to "Nonlinear," or "Sigmoidal." Also contained within the upper-right section are the buttons and displays for calibrating the software prior to testing. Prior to data collection the system must be calibrated so the control scheme knows the upper and lower limits of intensity. This is done by adjusting the shaker voltage to the two extremes, allowing for the readings to settle, and then capturing the lower and upper ranges by using the "Get Min" or "Get Max" buttons respectively. For variable frequency testing, a trial frequency sweep is run before testing, allowing the minimum and maximum fields to populate automatically. A "Reset" button is also included to clear the values manually.

The lower-left section of the GUI has one plot to display the shaker's input waveform. This allows the user to verify frequency, and amplitude of the signal being applied to the shaker. Below this plot is a numeric control which accepts an input voltage from 0 Vpp to 2 Vpp for use with the shaker. A visual indicator is included to alert the user when the shaker is running. Also included are three buttons which: trigger the frequency sweep during VF testing as well as two buttons which switch the controller between CF and VF calibration ranges.

The bottom-middle section has two plots which display the measured membrane pressure with sampled intensity (top) as well as the sinusoidal and sampled intensity (bottom). These plots allow the user to verify whether or not the synchronization subsystem and intensity sampling subsystems are working properly. If functioning correctly, the waveforms in the top plot will display in-phase while the sampled intensity will follow along the peaks of the sinusoidal intensity in the bottom plot.

The final two plots in the bottom-right section display membrane pressure (top) and membrane velocity (bottom). These waveforms will display as a sinusoid if functioning correctly since they are driven by the shaker. The final control box is simply test parameters for recording such as: length of recording, capture variables, when to trigger, and where to save.

3.5 Data Analysis

Following the collection of all data, various processing steps were taken to enhance the useful information without discounting the data set as a whole. A summary of the steps used can be seen below, while details and the rational behind each step will follow.

1. Time average all data between similar tests (i.e. Current data for all BS with nonlinear control at 1.5 Vpp shaker voltage in constant frequency testing)
2. Fast Fourier Transforms on data
3. Filter Data
    (a) Constant Frequency (100 Hz Excitation Data)
        i. Remove non-zero offsets in data
        ii. 9th order low-pass Butterworth filter with 125 Hz cut-off
        iii. Optional band-pass Butterworth filter between 95-105 Hz
        iv. 2nd order band-stop Butterworth filter at 60 Hz
    (b) Variable Frequency (0-300 Hz Excitation Data)
        i. Remove non-zero offset in data
        ii. 9th order low-pass Butterworth filter with 325 Hz cut-off
        iii. 2nd order band-stop Butterworth filter at 60 Hz
4. Spectral Analysis (Autocorrelations, Cross Power Spectral Densities, Coherence)
    (a) Constant Frequency (100 Hz Excitation Data)
        i. Perform autocorrelation analysis on current data.
        ii. Perform coherence analysis on data
    (b) Variable Frequency (0-300 Hz Excitation Data)
        i. Perform cross power spectral density analysis
        ii. Perform coherence analysis on data

3.5.1 Time Averaging

As alluded to in sections 3.3.4 and 3.3.5 the first step in processing the data is to time average the data between like trials. The reason for this is simply to reduce the influence of random noise in the data. Following this averaging, the magnitude of random noise in the data should be attenuated.

3.5.2 Fast Fourier Transforms

Fast Fourier transforms (FFTs) were used to help design the appropriate filters for the next step in signal processing. The FFTs on AHC current data were useful in verifying the excitation frequency for the constant frequency tests, as well as identifying additional unwanted frequency content such as 0 Hz constant offsets in the data as well as 60 Hz electromagnetic interference. This unwanted content appeared in the FFT plots as distinct peaks at 0 and 60 Hz respectively.

3.5.3 Filtering

Filtering the data is the second step in data processing. While several steps were taken during data collection to preserve fidelity of the signals in the frequency ranges of test, additional steps are needed to extract the information of interest. First, it is necessary to remove non-zero offsets in the data. These offsets generate significant 0 Hz spectral content that can adversely influence the useful information contained within the data. To do this, offsets in the data were removed simply by centering the data at zero.

Section 2.1 discusses the governing equations behind current generation in lipid bilayer systems and it is partly due to those equations that we have a need for low-pass filtering. Particularly in the test cases with a bilayer present, discrete changes in DC potential across the bilayer generate large capacitive current spikes. Jump discontinuities in DC potential force the $\frac{dV}{dt}$ term towards infinity, leading to large spikes in the time-domain data. However, these spikes are only momentary and contain high frequency content. Thus, applying the appropriate low pass filters can help reduce their influence on the data.

In the CF tests, a 9th-order low-pass Butterworth filter with a 125 Hz cut-off frequency was applied using MATLAB's ***filtfilt*** function to avoid introducing any unwanted phase shift in the data. This ***filtfilt*** command was used for all filtering steps unless indicated otherwise. Similarly, the VF tests use a 9th-order low-pass Butterworth filter with a 325 Hz cut-off frequency. The 9th-order filter was chosen for its flatness below 125Hz while having a sharp roll-off with minimal rippling.

Using the information from the FFTs, a notch filter, or band-stop filter, was designed to remove the narrow frequency band at 60 Hz in the AHC current data. While many precautions were taken to reduce the influence of electromagnetic interference in the data, the FFTs still indicated notable spectral content at 60 Hz. The 2nd-order Butterworth filter was designed to attain the maximum roll-off near 60 Hz without rippling.

3.5.4 Spectral Analysis

The next step in our data analysis is to investigate the spectral content of the signals and perform autocorrelation, cross power spectral density and coherence analyses on various portions of the data where appropriate. However, the data was first windowed using 5 or 15

Blackman-Harris windows, for constant frequency and variable frequency data respectively, with 50% overlap. Windowing the data prior to analysis is important to ensure that the analyzed signal appears periodic within the time range of interest to avoid excess spectral leakage. The number of points used per window was simply 2^x where x represents the next power of two greater than the length of each window. Since the number of windows results in section lengths of approximately 10,000 points, the next power of two is 14. Thus, the number of points used for each window was 2^{14} or 16,384.

For the constant frequency tests, autocorrelations were performed on the AHC current data for each test. This was done using MATLAB's ***cpsd*** function but supplying the AHC current data for both the "X" and "Y" inputs. Following these calculations, integrals were computed for each autocorrelation curve in the narrow-band 95-105Hz frequency range to obtain the mean squared power of each signal. An RMS power value was finally computed using these mean squared power values. Using this RMS power, plots were generated to compare the power output of the sensor at various intensity levels. This allowed us to observe any trends in the data caused by the application of the various control laws. The coherence between AHC current output and stinger velocity (fluid velocity) was also computed to verify the correlation between input excitation and output measurements.

For the variable frequency tests, cross power spectral densities were performed on the AHC current data and stinger velocity also using MATLAB's ***cpsd*** function. Unlike the constant frequency tests however, coherence plots rather than average values were generated across the excitation spectrum due to the broadband nature of the tests.

Chapter 4

Results and Discussion

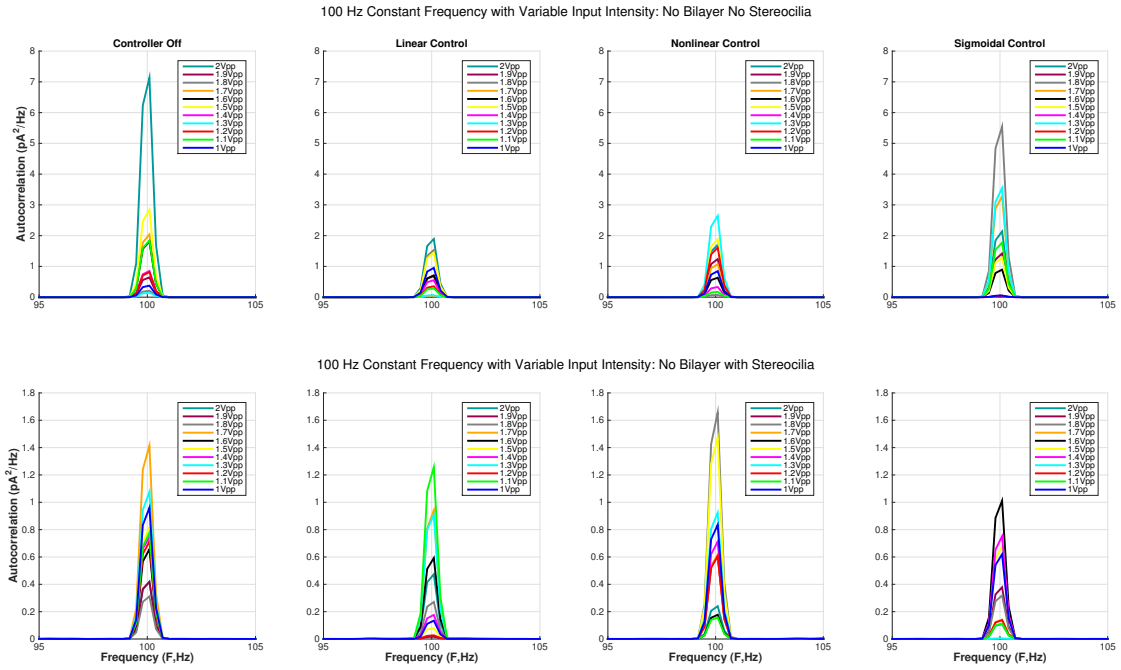
4.1 Constant Frequency Results

We have already stated that one of our research goals was to develop a control scheme which allows for adjustments to bilayer DC potential. After performing the tests as described in section 3.3.4, we looked at the results to see if the varying control laws had any impact amplifying or reducing the AHC current. To determine this we looked at the response of the system relative to the control cases where the bilayer was not subjected to any DC input. We also looked at the cases where no bilayer was present to ensure that the presence of a bilayer allowed for some degree of control. We expected to see increases in current output in cases where a bilayer was present, but unlike previous research where greater excitation levels lead to higher current outputs, we expected to see a more modest changes between excitation states. The reason being the varied DC potential across the bilayer as excitation levels changed. For smaller excitations we increased the DC potential in hopes of increasing

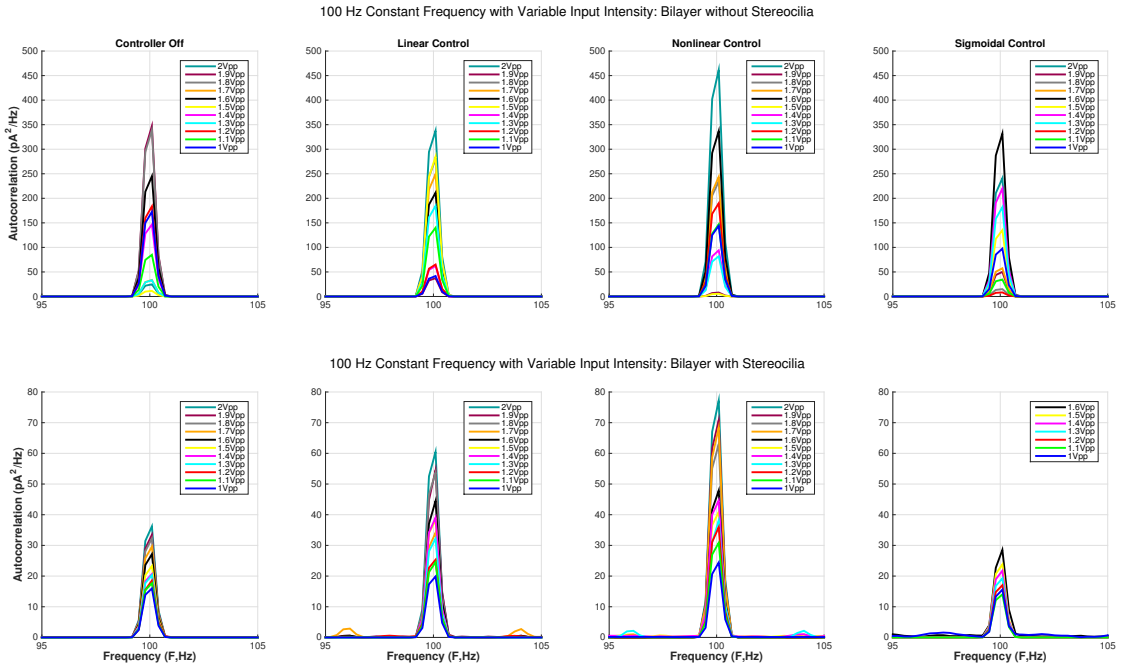
current output. Conversely, at high excitation levels we eliminated the DC potential to avoid amplifying the output any further. Thus, relative to the control cases where no control law was used, we expected to see larger increases in current output at low intensity levels and the same current outputs at high intensity levels. Figures 4.1a and 4.1b are the autocorrelation results for the no-bilayer and bilayer cases respectively.

For each of these plots, the response to the 11 different shaker input voltages are traced. We see quite clearly that the 100 Hz excitation appears as the most prominent peak in our data as expected. Viewing a wider range of frequency content shows several smaller peaks around the main 100 Hz peak, particularly in the cases where a bilayer was present, but the amplitudes were significantly smaller and likely noise generated by the shaker. Prior to processing the data, peaks at 0 and 60 Hz were the next most prominent points but were eliminated though careful filtering.

There are several observations we can make about the data presented above. First, as expected, the average current levels in the bilayer cases were much greater than those of the non-bilayer cases. As we are providing a conductive pathway, relative to the non-bilayer cases, this result makes sense. Yet, between bilayer cases, we see that the bilayer without a stereocilia case had the highest average outputs, two orders of magnitude greater than the no-bilayer cases and nearly an order of magnitude greater than the bilayer with stereocilia cases across the board. Likewise, between no-bilayer cases, we see the same result. The cases without a stereocilia provided higher current outputs. This is an intriguing observation which may be due in part to the additional mass of the stereocilia. While the stereocilia is designed to increase the amplitude of vibration experienced by the bilayer, it is possible that any increase in mechanical advantage is offset by the additional mass in the stereocilia tests. It may also be the case that the stereocilia was acting as a sort of tuned mass-damper,



(a)



(b)

Figure 4.1: Autocorrelation results between 95 and 105Hz for (a) the two cases where no bilayer is present and (b) the two cases where a bilayer is present. Each set has been scaled such that the y-axis is equivalent for plots of the same row, but changes between rows.

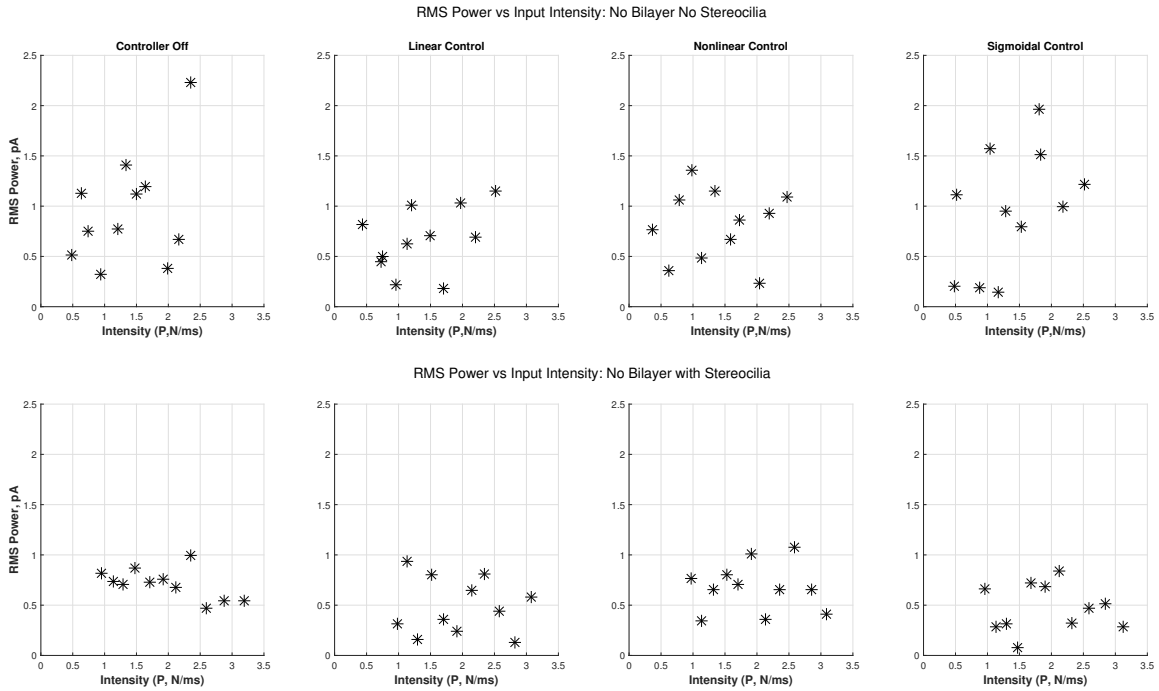
effectively keeping the vibrational energy away from the bilayer. With the direction of fluid flow parallel to the plane of the bilayer, it is also possible that maximum energy transfer was not achieved, as we expect normal forces to cause larger changes in bilayer area rather than shear forces which allow the droplets to slide against one another.

During the analysis, we computed the magnitude squared coherence values to correlate AHC current output with the fluid velocity inside the chamber. These calculations helped to determine whether or not the current output was in fact being driven by the excitation. Table 4.1 lists the average coherence values across all control states of the same test and their respective standard deviations.

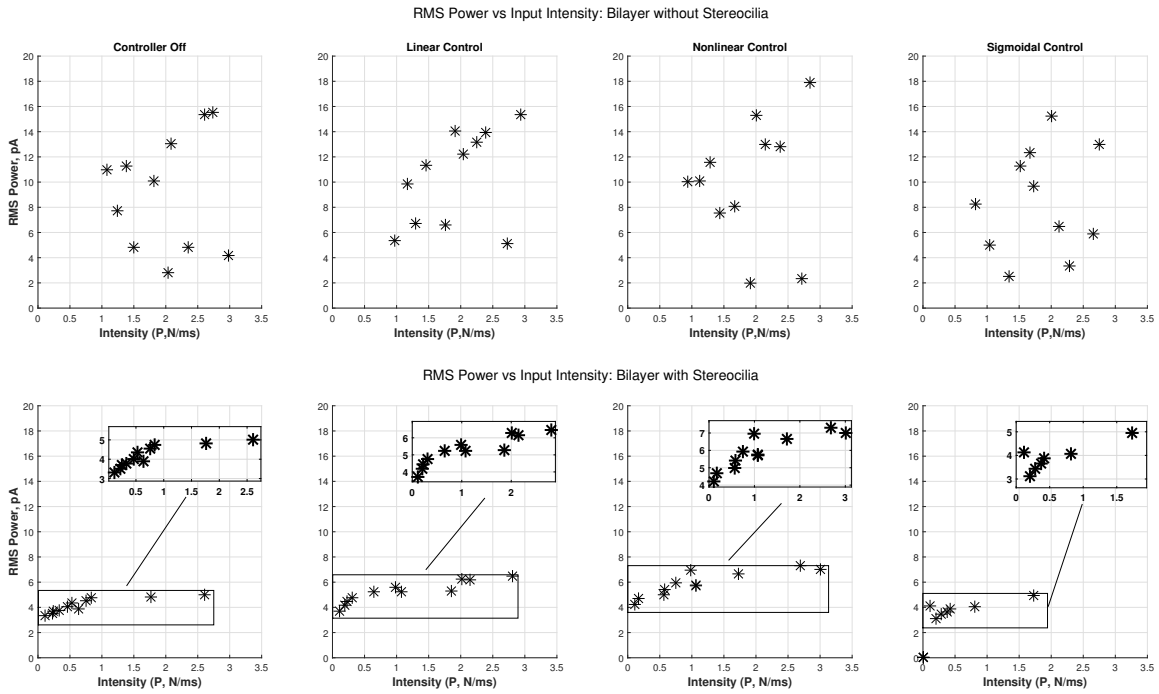
Table 4.1: Average Coherence and Standard Deviations for Constant Frequency Tests

	Average Coherence	**Standard Deviation**
No Bilayer No Stereocilia	0.9985	0.0029
No Bilayer with Stereocilia	0.9893	0.0266
Bilayer without Stereocilia	0.9972	0.0044
Bilayer with Stereocila	0.9952	0.0101

Our second hypothesis involved the changes in current output relative to the control cases. If we look at Figures 4.2a and 4.2b we can follow the changes of RMS power at different intensity levels from test to test. This will help determine whether the control laws implemented were able to increase current at lower intensity while maintaining current output at higher intensities, relative to the test case where no control mapping was used.



(a)



(b)

Figure 4.2: RMS current vs Input Intensity for (a) the two cases where no bilayer is present and (b) the two cases where a bilayer is present.

In the test cases where no bilayer was present, Figure 4.2a, there does not appear to be any distinct correlation between input intensity and RMS power. This is to be expected due to the open-circuit condition. In the bilayer cases of Figure 4.2b, we see no distinct correlation in the bilayer without stereocilia case. This is somewhat intriguing as we would have expected the changing DC potentials to have some effect on the sensor output. However, the RMS power during these tests was substantially higher than the non-bilayer cases. This is due to the introduction of a now conductive pathway across the lipid bilayer. The bilayer with stereocilia test cases are the only ones which provide some potential order in the results. Ideally what we expect to see are data points which are grouped at low intensity values along the x-axis increasing in power output during tests where the control law is active. Points grouped at higher intensities should have power outputs similar to the "controller off" state since less DC potential is being applied.

What we see is that the RMS power increases slightly with increasing intensity. This is true for all control states. Power within the various control state tests also remains similar in magnitude to the "controller off" state. This implies that the various control laws did not have a significant effect on the measured current output, and were not able to manipulate AHC current output in this particular configuration. However, it still appears as though the AHC sensors can respond to varying levels of mechanical excitation by outputting increased electrical current. In all test cases, RMS power increased by 50% or more from the lowest to highest intensity levels.

In our investigation, we also looked at the relationship strictly between the supplied voltage to the shaker (indicative of great excitation) and RMS power output. Since we expect the non-bilayer cases to have no correlation, we show only the bilayer cases in Figure 4.3 below.

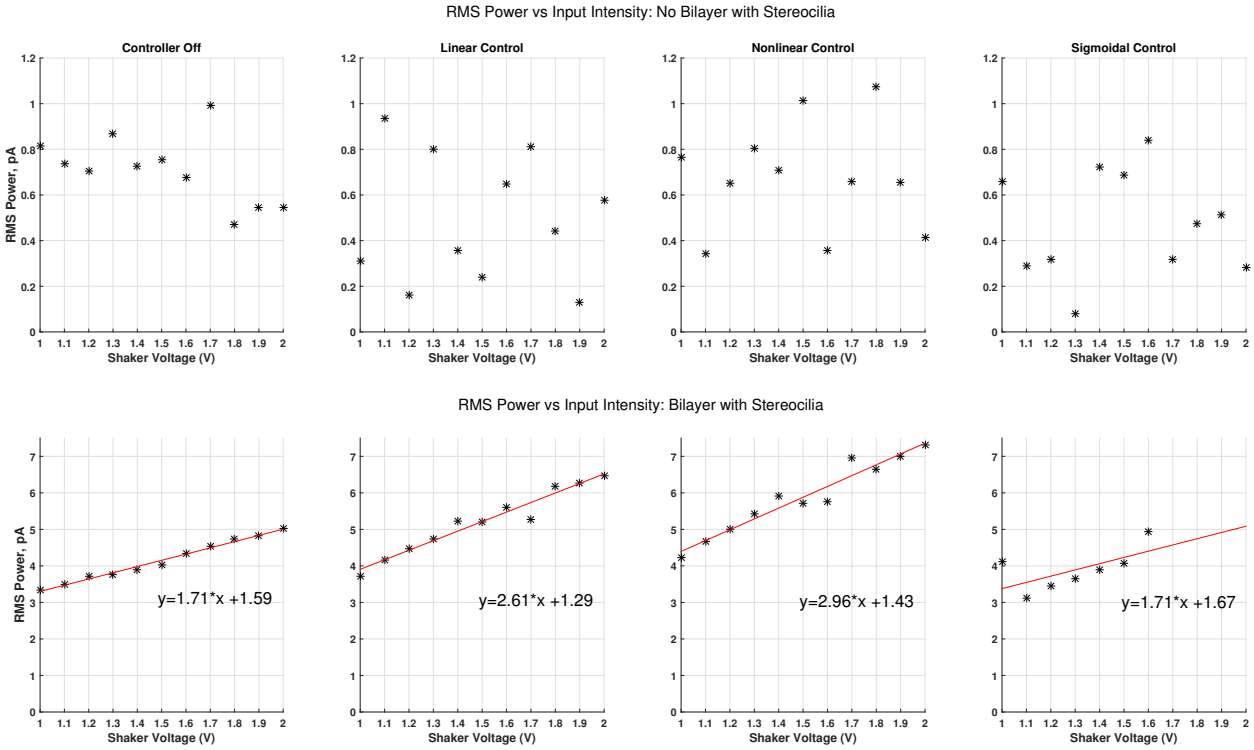


Figure 4.3: Plot of RMS power vs shaker voltage levels for only the cases where a stereocilia was present. Linear regressions are included for the bilayer with stereocilia case.

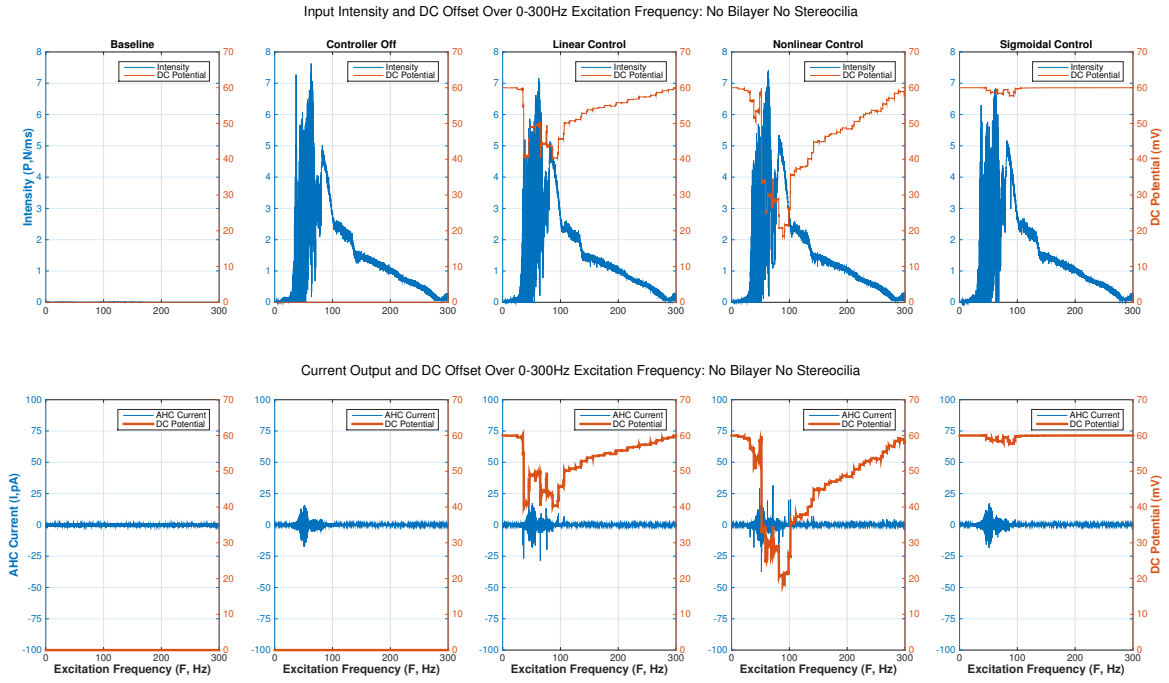
Here we see a more apparent trend in the bilayer with stereocilia test case versus the same plot from Figure 4.2b. Fitting a linear regression, we expect to see some difference in slope between the various control states which would indicate differing responses of the bilayer to certain DC mappings. We see that the nonlinear control mapping produces the largest slope: $m = 2.96\frac{pA}{V}$ followed by the linear control state with a slope of $m = 2.61\frac{pA}{V}$. Both the "controller off" and sigmoidal states have identical slopes of $m = 1.71\frac{pA}{V}$. Again, this is an interesting result. We expect the more aggressive mapping in the nonlinear control state to "compress" the slope of the resulting correlation. Instead, we see the opposite. One potential possibility could be the result of imperfect DC potential being held across the bilayer. While the excitation should be relatively constant, small changes in shaker output may generate larger discrete changes in DC potential due to the more aggressive mapping. These DC

changes may contribute to the $\frac{dV}{dt}$ term of equation 2.3 to produce greater current levels. As for the sigmoidal and "off" states being relatively similar, it is possible that the sigmoidal state never had the chance to reach the area of greatest change. Looking at Figure 3.16, we see that the sigmoidal curve has a very distinct plateau section, and falls below 90-percent of its maximum 60 mV value only after reaching a normalized intensity of 0.4. Since data was not available for the final four shaker voltages of the sigmoidal trial, it's possible that the most drastic changes in DC potential did not have the chance to occur. Ultimately, we do see some difference in the linear and nonlinear control state cases, but it appears as though these states had an effect on bilayer output opposite to what we intended. The fact that we see a more definitive trend between the relationship of RMS power to shaker voltage also indicates that our intensity calculation may be somehow "muffling" the bilayer responses.

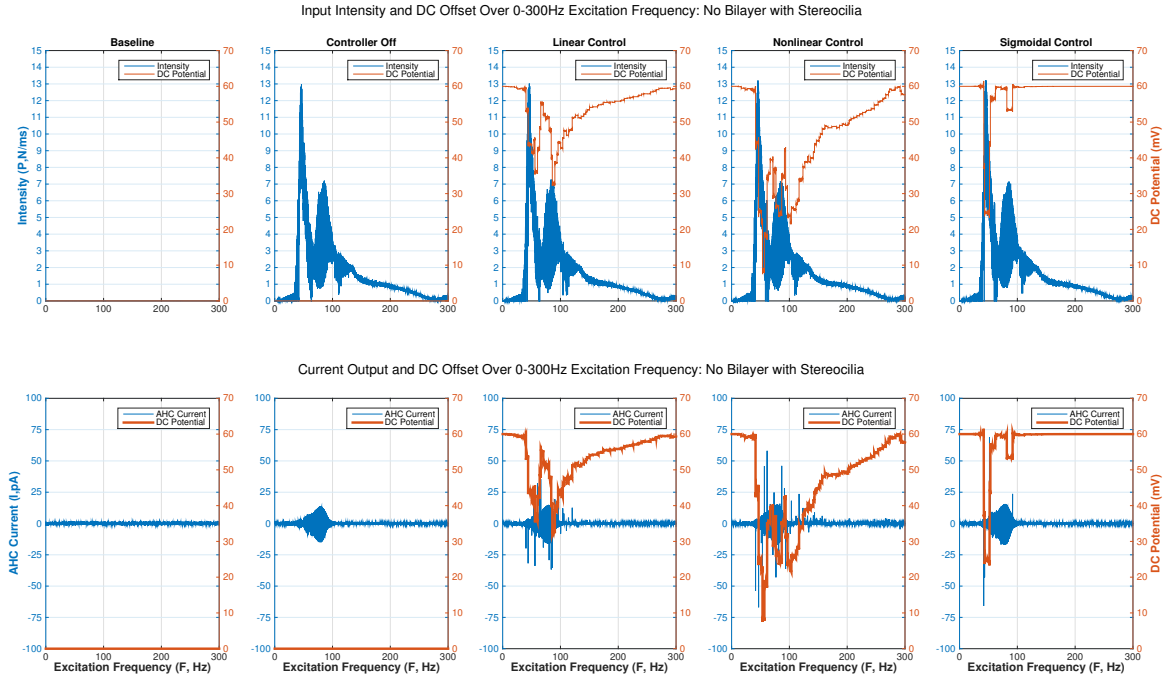
4.2 Variable Frequency Results

We now move to the results of the variable frequency testing. Unlike the constant frequency tests, we have included time-domain plots for the variable frequency results. We wanted to capture the transient response of the system to continually changing input intensities, thus plotting the AHC current response and DC potential traces simultaneously should allow us to view the effects of the DC controller on bilayer output. Figures 4.4 and 4.5 plot both the measured excitation intensity (top) and output current (bottom) during the broadband frequency sweep with the applied DC potential overlaid in orange. Figure 4.4 are the traces for the no bilayer conditions while Figure 4.5 provides the traces for both bilayer without a stereocilia and bilayer with stereocilia conditions.

What is immediately apparent in the time traces is the significant presence of high-amplitude current recordings, particularly in the two cases where a bilayer was present, Figure 4.5. These large amplitude spikes are capacitive noise triggered by the discrete changes in DC potential across the bilayer. If we recall equation 2.3, we see that the AHC current output is dependent on several variables. However, it is the $\frac{dV}{dt}$ term which is responsible for this capacitive noise. As the input intensity varies with excitation frequency, the sampled intensity value changes discretely at the specified sampling rate of 4 Hz. Several methods were employed to try and preserve the signal while reducing the capacitive noise. These included low-pass filtering, time averaging, multi-point moving averaging, and even peak elimination using both three and six sigma criteria. Unfortunately, none of the methods above yielded results that could be used in making accurate conclusions. This is further evidenced by looking at the coherence plots in Figure 4.7.

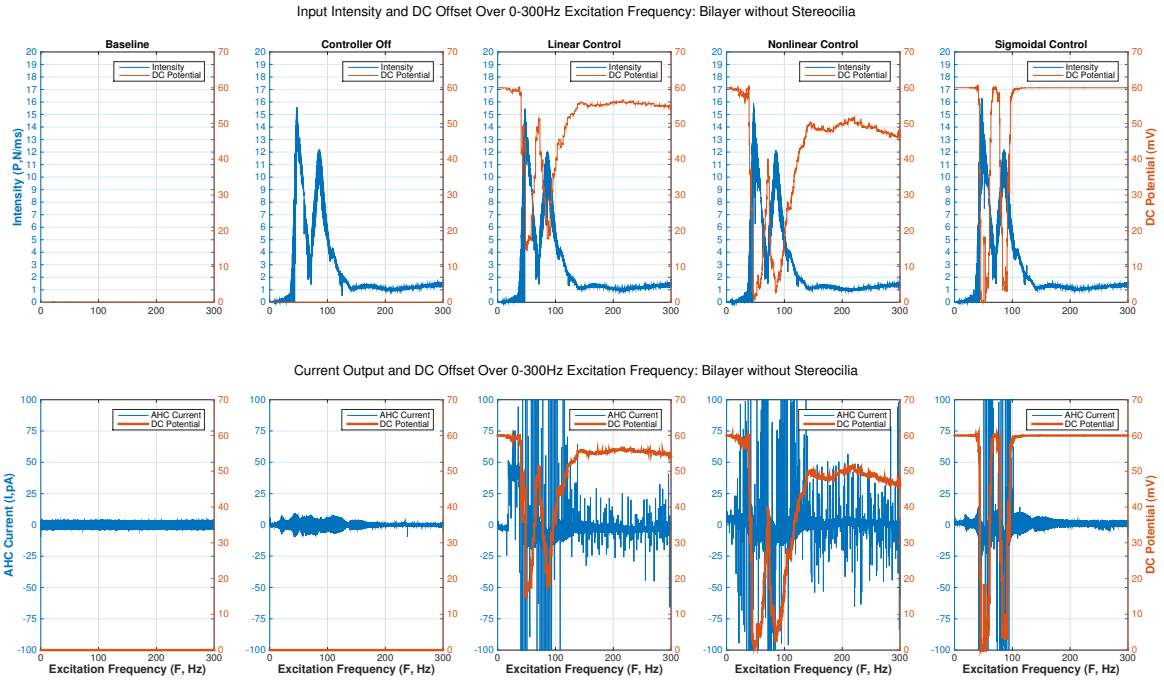


(a)

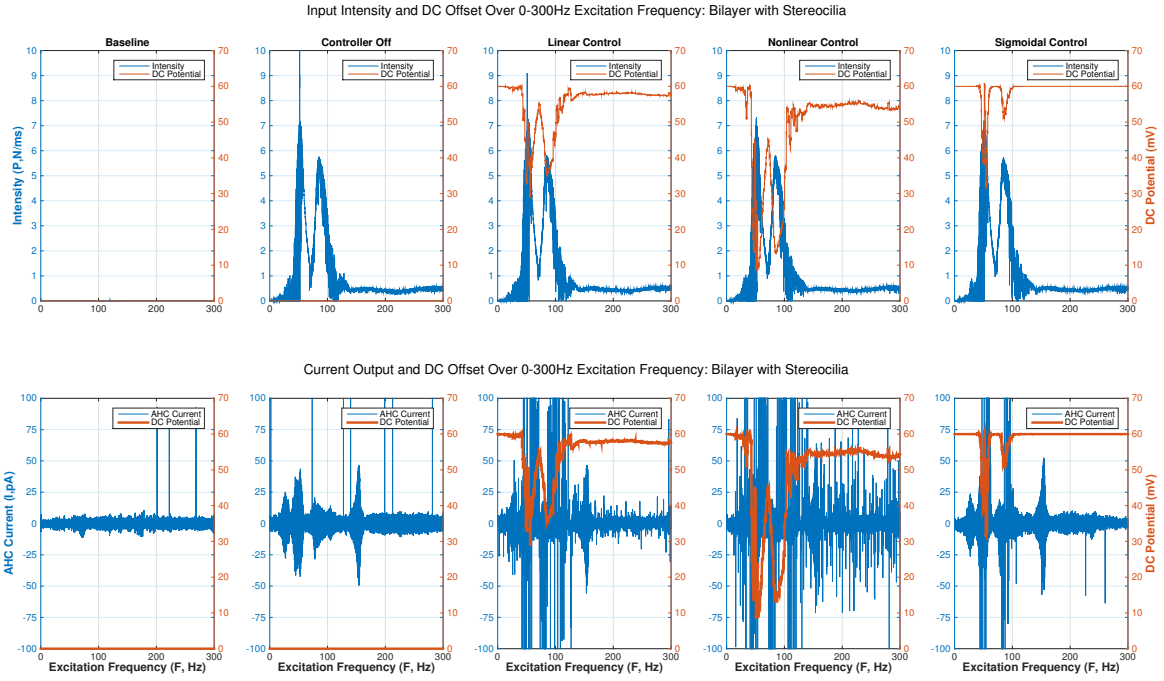


(b)

Figure 4.4: Time domain plots of excitation intensity, and current output with DC potential for: (a) No Bilayer No Stereocilia and (b) No Bilayer with Stereocilia cases.



(a)



(b)

Figure 4.5: Time domain plots of excitation intensity, and current output with DC potential for: (a) Bilayer without Stereocilia and (b) Bilayer with Stereocilia cases.

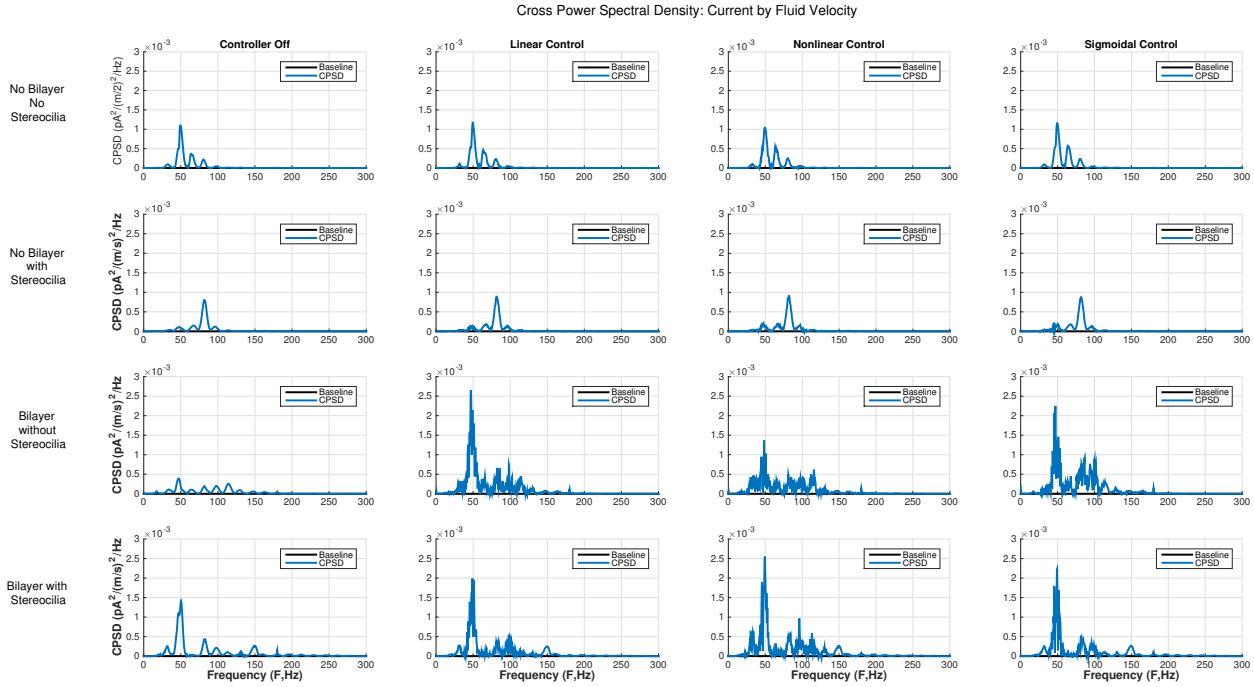


Figure 4.6: Cross power spectral density plots for each test variation. Scaled equally for easy comparison.

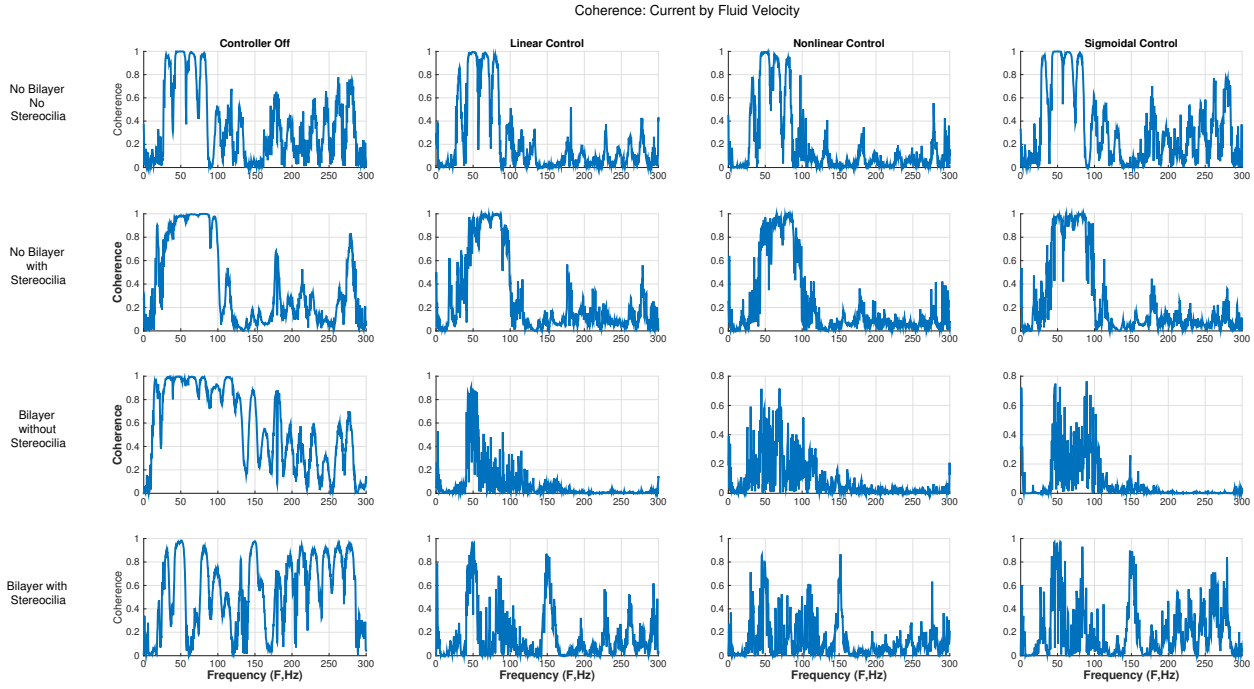


Figure 4.7: Coherence plots for each test case. Scaled equally for easy comparison.

With the exception of the test cases where a bilayer was present and a control law was being used, many of the coherence plots showed good coherence in the frequency range of 25 Hz to 100 Hz excitation. Beyond 100 Hz, the coherence dropped sharply to much lower levels, indicating that the relationship between fluid velocity and hair cell current was not well correlated. Ideally we would like to see good coherence levels across the excitation frequency spectrum, indicating that our hair cell sensor was responding the fluid velocity within the chamber.

The excessive noise described earlier could be one reason why coherence levels, for cases where a bilayer was present and a control law active, were much lower. It could be that the $\frac{dV}{dt}$ term of the governing electrical equation was the primary driver behind current generation. Additionally, due to the estimated resonant frequency of our hair cell being near 100 Hz, it is not completely unexpected to see some decrease in coherence levels at frequencies outside of resonance. Given all of these observations, we cannot conclude anything about the impact of our varying control law on sensor response. With that said, there are still some key points we can take away from these results.

First, we can see in each of the above figures that our open-loop control scheme is functioning as intended. This is most evident in the traces of DC potential over time. We see from the orange traces that as the measured intensity changes over time, with changing excitation frequency, the DC potential adapts in an inversely proportional manner. There are four significant events in which the input intensity dramatically increases to a peak, decreases to a valley, increases back to a peak and then finally decreases to a relatively constant level once more. At the same points we see the DC potential hit local minimums and maximums corresponding to the concurrent intensity level. We can also see the discrete step changes associated with the intensity sampling which unfortunately lead to the capacitive current

spikes.

Additionally, we can see three distinct patterns in the changing DC potential dictated by the mapping function used. The linear, non-linear, and sigmoidal mappings each have their own unique signature." While we cannot necessarily point to one particular mapping that is most useful, we can say that the changes in bilayer current do seem to be affected by the type of mapping used. This may prove useful as controller design improves and specific maps can be tailored to specific applications.

Unlike previous experiments within our group, these tests are changing the DC potential across the bilayer in a relatively quick and discrete fashion and not in-between tests where the bilayer is given time to reach a steady state. As such, it is possible that the bilayer is not reacting quickly enough to the voltage changes which should force a change in its surface area, and consequently the capacitance of the system.

Chapter 5

Summary and Conclusions

5.1 Summary of Work

5.1.1 Hair Cell and Testing Environment

Throughout the term of this project, we addressed several key challenges to reach our goal of implementing a control method for artificial hair cell sensors. Two of these challenges focused on the physical aspects of sensor design and test environment. What we achieved in these areas is important to the future progress of this work.

In regards to our artificial hair cell sensors, we have used a relatively new method of bi-layer manipulation which is centered around the use of micropipette electrodes acting as both instruments for electrical interrogation as well as physical manipulation. Rather than inserting Ag/AgCl wires directly into our aqueous droplets or hydrogel follicles, using glass micropipettes allows us the option of creating significantly smaller diameter electrodes in the

future while providing increased levels of control. Placing hydrogel droplets at the ends of these pipettes also provides an "anchor" of sorts for aqueous lipid droplets. Once droplets are anchored to the hydrogel, moving the glass pipettes allows us to subsequently move the attached droplets to achieve bilayer formation, separation or specific bilayer sizes.

The test environment in this work proved to me more of an evolutionary step over previous designs rather than revolutionary. As detailed back in sections 3.1.1 and 3.1.2, many design elements remained unchanged from previous work. Modifications were made to the chamber's flexible membrane to facilitate better energy transfer, and substrate components for use with the pipette based bilayer formation strategy.

5.1.2 Controller

In this work we have built the first iteration of an open-loop feed-forward controller to manipulate the DC offset across a lipid bilayer in a bio-inspired artificial hair cell sensor. The goal was to change the control law governing the DC potential in such a way as to begin mimicking the the non-linear tuning phenomenon observed in the human cochlea. By applying increased DC potentials across the bilayer we sought to amplify output current by utilizing the electrowetting effect to increase the surface area of our bilayer and subsequently increase the capacitance.

We observed that the controller did function as designed, sampling both the shaker force and velocity and processing these variables to obtain a single "intensity" value used to quantify the level of excitation experienced by the system. In our constant frequency tests we saw no significant impact of the various control laws on AHC current output. It does appear however, that the artificial hair cell sensor (bilayer with stereocilia) responded to increased

excitation intensities by outputting increased current levels. Between lowest and highest intensity excitation states, the AHC test case yielded 50% or more RMS power consistently from test to test. In our variable frequency tests, the intensity sampling unfortunately led to excessive capacitive noise in the data which did not allow us to draw any conclusions about the effect of the control law on bilayer current output. However, we were still able to visually identify distinct response signatures between the three different DC mappings: linear, non-linear, and sigmoidal.

It seems as though the controller we designed and implemented has promise for future use as long as a few key improvements are made to aid in consistency and reduce the secondary effects of discrete intensity sampling.

5.2 Future Work and Improvements

With the work here being just the beginning of a long term aspiration to develop bio-inspired artificial hair cell sensors for use in cochlear devices or smart materials, there are a number of different avenues which can be pursued to continue making progress towards this goal. Several near-future areas for investigation include aspects such as: fabrication methods, chamber design, material usage, and software improvements.

To create an artificial cochlear device, which utilizes artificial hair cell sensors similar to those described in this work, significant size reductions are necessary. During the early phases of this work, various fabrication methods were investigated with some success. For example, we were able to achieve glass filament diameters of several microns in diameter, with lengths over 50μm using a flaming brown pipette puller. However, manipulating and controlling these

filaments in such a way as to create an artificial hair cell system were unsuccessful. This was likely a result of our limited fabrication capabilities at the time and may be addressed by certain MEMS processes.

Chamber design is another area that would benefit from future work. The set-up used here was designed to accept a direct shaker input which, in-turn, would generate an oscillatory fluid flow around the stereocilia element of the AHC. Ideally, the fixture containing the AHCs would be sensitive enough to pick up acoustic signals and transmit those signals, without loss, to the contained fluid. Additionally, it is important to isolate unwanted vibration. Because the bilayer systems used here generate current in a manner directly proportional to bilayer surface area, unwanted vibration may induce undesirable changes in bilayer size and subsequently provide false readings. In this work, great care was taken to reduce vibration of the chamber through the use of damping materials and clamps. However, there is likely further improvements that can be made in this area as some vibration could still be seen.

One last area which could benefit greatly from further investigation is that of the controller software. With this work being the first of its kind, the controller built here simply represents a foundation from which to build. Nearly every portion of the control scheme used here could benefit from some form of improvement. Areas for improvement range from the very first input filtering functions all the way to the final output rate. Specific areas which could benefit greatly include more specialized gain functions, and smoothing of the DC offset curves. The human cochlea has a very sharp tuning curve which doesn't quite match the trio of functions implemented here and the current sampling scheme for DC offsets leads to frequent jump discontinuities in holding potential. These quick changes lead to large current spikes in the data which could be resolved with some type of predictive curve smoothing function.

Appendix A

Test Chamber Specifications

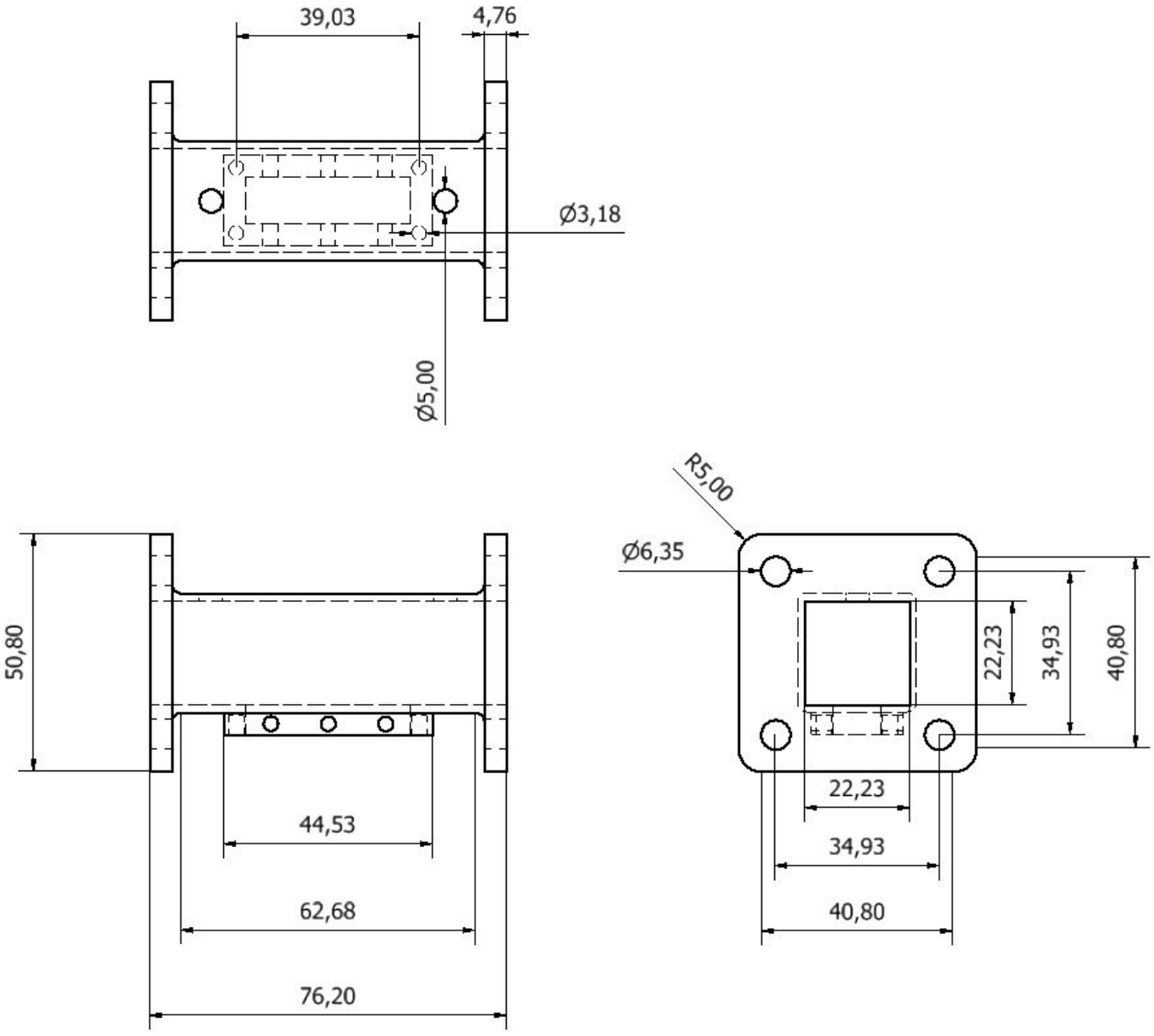


Figure A.1: Detailed drawing of the main body for the test environment. It is comprised of an acrylic tube mated to two enplates where the membrane is held in place by a second set of endplates (not pictured).

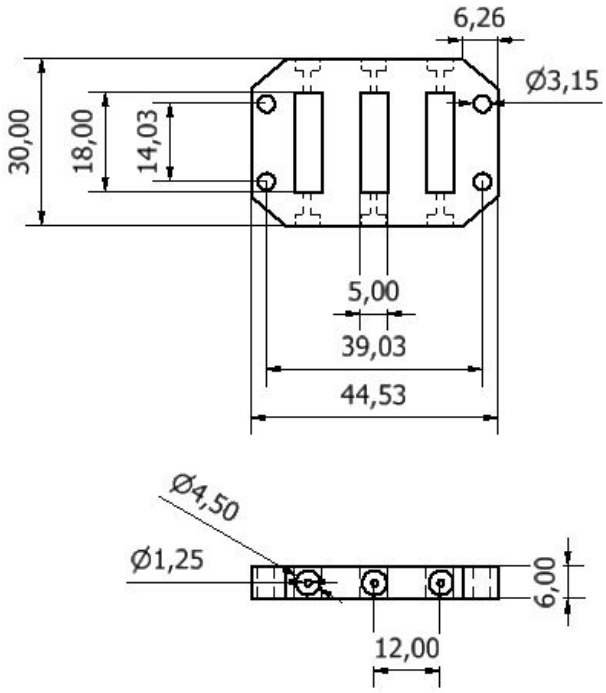


Figure A.2: The "extended" substrate use to contain the artificial hair cell sensors. Countersunk holes provide areas for rubber gaskets to seal the test environment, preventing leaks.

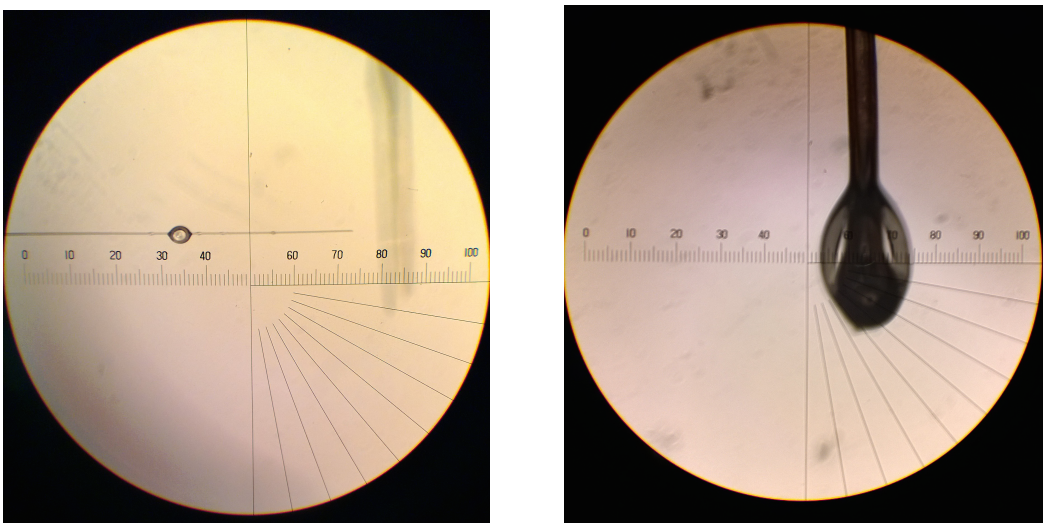
Appendix B

Miniaturization Work

Prior to settling on the controller as the primary aspect of this work, there was a great deal of time and effort devoted in attempting to fabricate artificial hair cell sensors that had dimensions similar to those of actual biologic hair cells. We attempted to achieve stereocilia lengths on the order of 10μm, diameters of less than 5μm, and hair cell body sizes of approximately 50μm.

Using a flaming brown pipette puller, these stereocilia diameters were well within our fabricating capability. Using the resulting pipette output from the flaming brown puller, we used a Narshige micro-forge to tailor the length and shape of the newly formed glass fibers. The result was a borosilicate structure with dimensions somewhat larger than a biologic hair cell but several orders of magnitude less than previous fabrication attempts. An example of this type of structure can be seen in Figures B.1a and B.1b.

The greatest difficulty came when trying to assemble the entire hair cell structure and manipulate it accordingly. We needed to have a hydrogel base to anchor our aqueous lipid



(a) (b)

Figure B.1: (a) Example of a prototype artificial hair cell structure under Narshige microforge. A hydrogel droplet is cured along the length to form an anchor for aqueous lipid solution (b) A close up shot of another prototype artificial hair cell structure with hydrogel anchor.

droplets. Attempts to simply surround the base of the glass structure with an aqueous lipid solution, and excite the stereocilia did not induce any measurable current output in the system. Some success in providing a hydrogel base was made, but we were also faced with the challenge of being able to manipulate the structure in such a way that we could stabilize the structure.

As biologic hair cells are embedded in the cellular matrix of the organ of Corti, attempts were made to encapsulate these structures in a polyurethane substrate. This is quite similar to the process used by others in our group, namely Sarles. However, limitations of our current equipment did not allow for enough control in this area. The small structures could not be contained appropriately or would often break during any attempts to move them. Additionally, the equipment required to accurately probe these small structures significantly limited the design freedom to excite and view each structure. Typically, several microma-

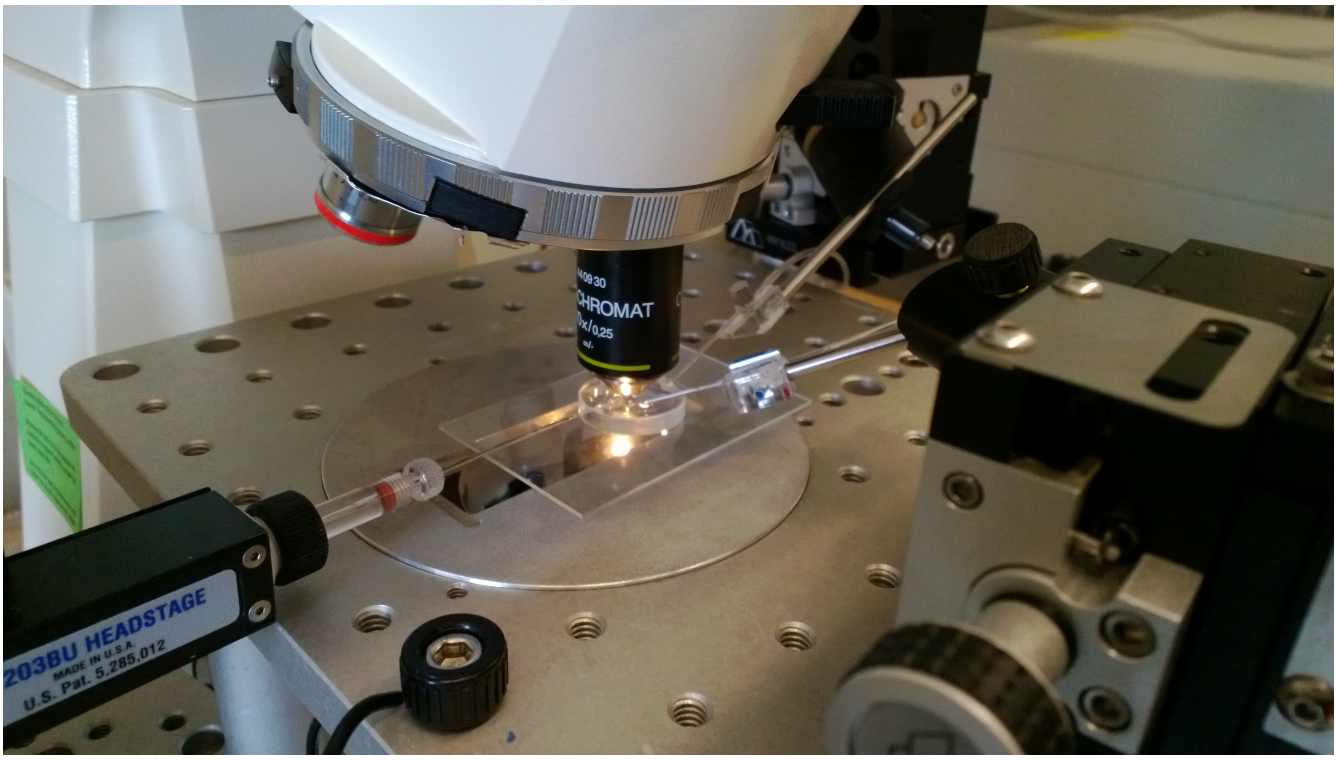


Figure B.2: Preliminary test set-up involving micro scaled droplets and hair cell structures.

nipulators were required to stabilize the electrodes while also providing extremely small volumes of lipids for bilayer formation. Even when situated on a vibration isolation table, small environmental changes could easily hamper efforts to maintain a bilayer when using the stereocilia like structures. An example of the early test setup with micromanipulators can be seen below in Figure B.2.

With that said, we were able to achieve bilayer formation and measurements between aqueous droplets with diameters $< 50\mu$m on several occasions when not attempting to make a complete AHC device. This at least verifies the measurement and recording capabilities of our equipment.

To achieve sensor sizes similar to biologic hair cells of the cochlea, MEMS processes may

likely be required. One thought may be to use deep reactive ion etching (DRIE) to create small cantilevered hair-like stereocilia structures. Assuming these structures could be formed on top of an embedded circuit within the silicon wafer, the stereocilia could double as the interrogating electrode required for electrical recordings. The last step would be to create a hydrogel base that would vibrate with the stereocilia, allowing vibrational energy to be transferred from the cantilevered protrusion to the lipid bilayer.

Bibliography

[1] *Encyclopedia Britannica. Encyclopedia Britannica Online.* Encyclopedia Britannica Inc., 2015. Web. 11 Jan. 2015 http://www.britannica.com/

[2] National institute on deafness and other communication disorders (nidcd), October 3, 2014 2014.

[3] J. Ashmore, P. Avan, W. E. Brownell, P. Dallos, K. Dierkes, R. Fettiplace, K. Grosh, C. M. Hackney, A. J. Hudspeth, F. Jülicher, B. Lindner, P. Martin, J. Meaud, C. Petit, J. R. Santos Sacchi, and B. Canlon. The remarkable cochlear amplifier. *Hearing Research*, 266(1–2):1–17, 2010.

[4] Hagan Bayley, Brid Cronin, Andrew Heron, Matthew A. Holden, William L. Hwang, Ruhma Syeda, James Thompson, and Mark Wallace. Droplet interface bilayers. *Molecular BioSystems*, 4(12):1191–1208, 2008.

[5] Clopton Ben and Voigt Herbert. *Auditory System*, pages 39934–39950. Electrical Engineering Handbook. CRC Press, 2006. doi:10.1201/9781420003857.ch5.

[6] Amitava Biswas. A novel analysis of the mechanics of cochlea, the inner ear. *ASME Conference Proceedings*, 2003(37106):119–120, 2003.

[7] Stephen Bolsover. *Cell Biology: A Short Course*. Wiley-Blackwell, Hoboken, NJ, 3 edition, 2011.

[8] P. Dallos. The active cochlea. *The journal of neuroscience*, 12(12):4575–4585, 1992.

[9] PETER Dallos. Response characteristics of mammalian cochlear hair cells. *The Journal of neuroscience*, 5(6):1591–1608, 1985.

[10] Wei Dong and Elizabeth Olson. Detection of cochlear amplification and its activation. *Biophysical Journal*, 105(4):1067–1078, 2013.

[11] H. Engström and B. Engström. Structure of the hairs on cochlear sensory cells. *Hearing research*, 1(1):49–66, 1978.

[12] Chien Fan and Bei-Tse Chao. Unsteady, laminar, incompressible flow through rectangular ducts. *Zeitschrift für angewandte Mathematik und Physik ZAMP*, 16(3):351–360, 1965.

[13] Robert Fettiplace. Electrical tuning of hair cells in the inner ear. *Trends in Neurosciences*, 10(10):421–425, 1987.

[14] Å. Flock and S. Orman. Micromechanical properties of sensory hairs on receptor cells of the inner ear. *Hearing research*, 11(3):249–260, 1983.

[15] K.L. Garrison, S.A. Sarles, and D.J. Leo. Formation, encapsulation, and validation of membrane-based artificial hair cell sensors. In *Proceedings of SPIE*, volume 8339, page 83390B.

[16] JH Gerrard and MD Hughes. The flow due to an oscillating piston in a cylindrical tube: a comparison between experiment and a simple entrance flow theory. *Journal of Fluid Mechanics*, 50(01):97–106, 1971.

[17] Peter G. Gillespie and Ulrich Müller. Mechanotransduction by hair cells: Models, molecules, and mechanisms. *Cell*, 139(1):33–44, 2009.

[18] Michael P. Gorga, Stephen T. Neely, Darcia M. Dierking, Judy Kopun, Kristin Jolkowski, Kristin Groenenboom, Hongyang Tan, and Bettina Stiegemann. Low-frequency and high-frequency cochlear nonlinearity in humans. *The Journal of the Acoustical Society of America*, 122(3):1671–1680, 2007.

[19] Donald D. Greenwood. Cochlear nonlinearity and gain control as determinants of the response of primary auditory neurons to harmonic complexes. *Hearing Research*, 32(2–3):207–253, 1988.

[20] John J. Guinan Jr. How are inner hair cells stimulated? evidence for multiple mechanical drives. *Hearing Research*, 292(1–2):35–50, 2012.

[21] John J. Guinan Jr. New insights into cochlear amplification. *Biophysical Journal*, 105(4):839–840, 2013.

[22] B. Harland, W.E. Brownell, A.A. Spector, and S.X. Sun. Voltage-induced bending and electromechanical coupling in lipid bilayers. *Physical Review E*, 81(3):031907, 2010.

[23] M.A. Holden, D. Needham, and H. Bayley. Functional bionetworks from nanoliter water droplets. *Journal of the American Chemical Society*, 129(27):8650–8655, 2007.

[24] Robert Hooke. Micrographia: or some physiological descriptions of minute bodies made by magnifying glasses with observations and inquires therupon. 1665.

[25] A. J. Hudspeth. Making an effort to listen: Mechanical amplification in the ear. *Neuron*, 59(4):530–545, 2008.

[26] AJ Hudspeth. The hair cells of the inner ear. *Scientific American*, 1983.

[27] A.J. Hudspeth. How the ear's works work. *Nature*, 341(6241):397–404, 1989.

[28] G Iliadis and P Anagnostopoulos. Viscous oscillatory flow around a circular cylinder at low keulegan–carpenter numbers and frequency parameters. *International journal for numerical methods in fluids*, 26(4):403–442, 1998.

[29] Shuping Jia, Peter Dallos, and David ZZ He. Mechanoelectric transduction of adult inner hair cells. *The Journal of neuroscience*, 27(5):1006–1014, 2007.

[30] Meredith LeMasurier and Peter G. Gillespie. Hair-cell mechanotransduction and cochlear amplification. *Neuron*, 48(3):403–415, 2005.

[31] J. S. Lighthill. Biomechanics of hearing sensitivity. *Journal of vibration, acoustics, stress, and reliability in design*, 113(1):1, 1991.

[32] D.J. Lim. Functional structure of the organ of corti: a review. *Hearing research*, 22(1):117–146, 1986.

[33] Joseph Najem, Myles Dunlap, Sergei Sukharev, and Donald J Leo. Mechanosensitive channels activity in a droplet interface bilayer system. *MRS Proceedings*, 1621:mrsf13–1621–d01–05, 2014.

[34] Alexander G. Petrov. Electricity and mechanics of biomembrane systems: Flexoelectricity in living membranes. *Analytica Chimica Acta*, 568(1–2):70–83, 2006.

[35] Preston A Pinto. Novel bio-inspired aquatic flow sensors. Technical report, DTIC Document, 2012.

[36] Luis Robles and Mario A Ruggero. Mechanics of the mammalian cochlea. *Physiological reviews*, 81(3):1305–1352, 2001.

[37] Mario A Ruggero, Nola C Rich, Alberto Recio, S Shyamla Narayan, and Luis Robles. Basilar-membrane responses to tones at the base of the chinchilla cochlea. *The Journal of the Acoustical Society of America*, 101(4):2151–2163, 1997.

[38] K.T. Sapra and H. Bayley. Lipid-coated hydrogel shapes as components of electrical circuits and mechanical devices. *Scientific Reports*, 2, 2012.

[39] S.A. Sarles and D.J. Leo. Hair cell sensing with encapsulated interface bilayers. In *Proceedings of SPIE*, volume 7975, page 797509.

[40] S.A. Sarles and D.J. Leo. Membrane-based biomolecular smart materials. *Smart materials and structures*, 20(9):094018, 2011.

[41] S.A. Sarles, J.D.W. Madden, and D.J. Leo. Hair cell inspired mechanotransduction with a gel-supported, artificial lipid membrane. *Soft Matter*, 7(10):4644–4653, 2011.

[42] Stephen A. Sarles and Donald J. Leo. Cell-inspired electroactive polymer materials incorporating biomolecular materials. pages 797626–797626, 2011. 10.1117/12.881703.

[43] Rodrigo Sarlo and Donald Leo. Directional sensitivity analysis of a hydrogel-supported artificial hair cell. In *ASME 2013 Conference on Smart Materials, Adaptive Structures and Intelligent Systems*, pages V002T06A016–V002T06A016. American Society of Mechanical Engineers.

[44] Charles R. Steele and Sunil Puria. Force on inner hair cell cilia. *International Journal of Solids and Structures*, 42(21–22):5887–5904, 2005.

[45] Nima Tamaddoni and Andy Sarles. Fabrication and characterization of a membrane based hair cell sensor that features soft hydrogel materials. In *ASME 2012 Conference on Smart Materials, Adaptive Structures and Intelligent Systems*, pages 565–571. American Society of Mechanical Engineers.

[46] Nima J. Tamaddoni, Christopher P. Stephens, and S. A. Sarles. Fabricating neuromast-inspired gel structures for membrane-based hair cell sensing. pages 833908–833908, 2012. 10.1117/12.915203.

[47] Jeffrey P Travis, Myles D Dunlap, Donald J Leo, and J Wallace Grant. Dynamic characterization of biomimetic artificial hair cells. In *ASME 2013 Conference on Smart Materials, Adaptive Structures and Intelligent Systems*, pages V002T06A011–V002T06A011. American Society of Mechanical Engineers.

[48] Jeffrey Philip Travis. *Design and Characterization of Biomimetic Artificial Hair Cells in an Artificial Cochlear Environment*. PhD thesis, 2014.

[49] Gabriel Villar, Alexander D. Graham, and Hagan Bayley. A tissue-like printed material. *Science*, 340(6128):48–52, 2013.

[50] Ernest Glen Wever and Merle Lawrence. Physiological acoustics. 1954.

[51] Stephen H. White and T. E. Thompson. Capacitance, area, and thickness variations in thin lipid films. *Biochimica et Biophysica Acta (BBA) - Biomembranes*, 323(1):7–22, 1973.

[52] Misato Yamada, Hiromasa Imaishi, and Kenichi Morigaki. Microarrays of phospholipid bilayers generated by inkjet printing. *Langmuir*, 29(21):6404–6408, 2013.